Effect of sub-boundaries on primary spacing dynamics during 3D directional solidification conducted on DECLIC-DSI

F.L. Mota, J. Pereda, K. Ji, Y. Song, R. Trivedi, A. Karma, N. Bergeon

Effect of sub-boundaries on primary spacing dynamics during 3D directional solidification conducted on DECLIC-DSI

F.L. Mota[a], J. Pereda[a], K. Ji[b], Y. Song[b1], R. Trivedi[c], A. Karma[b], N. Bergeon[a]*

[a] *Institut Matériaux Microélectronique Nanosciences de Provence, Aix-Marseille Université and CNRS UMR 7334, Campus Saint-Jérôme, Case 142, 13397 Marseille Cedex 20, France*

[b] *Department of Physics and Center for Interdisciplinary Research on Complex Systems, Northeastern University, Boston, Massachusetts 02115, USA*

[c] *Department of Materials Science and Engineering, Iowa State University, Ames, Iowa 50010, USA*

Abstract

To characterize the dynamical formation of three-dimensional (3D) arrays of cells and dendrites under diffusive growth conditions, *in situ* monitoring of a series of experiments on a transparent *succinonitrile* – 0.24 wt% *camphor* model alloy was carried out under low gravity in the DECLIC Directional Solidification Insert onboard the International Space Station. The continuous interface observation enables to construct space-time evolution maps of cell location and primary spacing. Both convergent and divergent sub-boundaries are identified and new insights on their effects on the spatiotemporal evolution of the pattern are thus evidenced. 3D phase-field simulations that reproduce the experimental sub-boundary configurations are performed to support the analyses. Even for the low angle sub-boundaries studied, the primary spacing increases or decreases in the vicinity of the boundary respectively for divergent and convergent sub-boundary. This effect may extend on a long distance within the different sub-grains and its magnitude depends on the average primary spacing and its positioning relative to the limits of the stability band. On the sample scale, the primary spacing profile is also influenced by the presence of sources and sinks at the crucible wall due to the pattern drift. Their type and distance from the sub-boundaries give rise to complex spatial distributions of primary spacing over the entire sample.

Keywords: directional solidification, microgravity experiments, phase-field simulation, pattern formation, sub-boundaries

* nathalie.bergeon@im2np.fr
+33 (0)4 13 94 52 53

1: Present address for Y. Song : Computational Science and Engineering Division, Oak Ridge National Laboratory, Oak Ridge, TN, United States.

1. Introduction

The study of solidification microstructure formation and selection is crucial to engineering and to the processing of advanced new materials. Solidification is also a typical model of nonlinear pattern formation [1]. One of the key problems in pattern evolution is the prediction of the specific pattern developed under given growth conditions, cellular or dendritic, and of its characteristics such as its primary spacing. Pattern selection occurs under dynamic conditions of growth in which the unstable pattern goes through the process of reorganization into a rather periodic array.

Pattern selection has been theoretically and experimentally studied, mainly in thin-sample geometries [2-9]. Numerous studies were directed at predicting the morphological characteristics, and especially the primary spacing, of growing patterns as a function of controlling growth parameters [2, 8, 10, 11]. However, following the development of the Warren & Langer model [12], it has been progressively recognized through experiments and theoretical/numerical analyses that a wide band of stable spacings exists and that the selection of primary spacing is history-dependent [4, 7, 8, 13-17]. The lower limit of the stable spacing band is defined by the elimination instability, while its upper limit is due to tertiary branching (dendritic array) or tip-splitting (cellular array) instabilities. Elimination or formation of a new cell/dendrite are local phenomena that also affect the primary spacing of neighboring structures. For example, a tip-splitting may propagate step-by-step to reduce the spacing after a velocity jump [7] or a local change of spacing induced by an elimination is distributed over neighboring cells by lateral motions [8]. In a large real sample, variations or heterogeneities of spacing do not only come from the extent of the band of stable spacings: they may result from macroscopic defects such as interface curvature [18, 19], presence of convection effects [20-24], or presence of several grains associated to different growth directions [25-29]. Moreover, in case of misorientation, the pattern is travelling due to the tilt of the growth direction [29, 30], thus inducing a process of source and sink of structures; the source may emit structures of spacing different than the average intra-grain spacing and it was recently demonstrated that in that case, a propagative mechanism of spacing selection then operates on large space and time scales [31].

In situ observation of the solid-liquid interface is a precious tool to get a detailed knowledge of the entire time-evolution of the interface pattern. Transparent organic analogs [32] have been widely used for such in situ observation but mainly in thin sample geometry. Even if such configurations have led to very large progress in understanding the dynamics of solidification [3, 5, 11, 30, 33, 34], they do not perfectly represent 3D samples and quantitative data extracted from 2D systems cannot be extrapolated to 3D ones [17, 35, 36]. The main problem to study 3D samples comes from the presence of significant convection under the growth conditions which give rise to cellular and dendritic structures. Fluid flow modifies the structure of the solute boundary layer by sweeping thus causing non-uniform morphological instability with the formation of a non-uniform microstructure and, as previously mentioned, non-uniform primary spacing [20-24, 37, 38]. Thin samples geometry is the easiest method to avoid or drastically reduce convection, however, keeping 3D samples demands the reduced-gravity environment of space to eliminate fluid flow.

The studies presented here were conducted using the Directional Solidification Insert (DSI) dedicated to *in situ* and real time characterization of the dynamical selection of the solid-liquid interface morphology on BULK samples of transparent materials. It was developed by the French Space Agency (CNES) in the frame of the DECLIC project (DEvice for the study of Critical LIquids and Crystallization) and was installed within the International Space Station (ISS) in 2010-2011 to benefit from a microgravity environment. Experiments performed on DECLIC-DSI led, for example, to unprecedented observations of breathing-mode oscillations in spatially extended cellular arrays [39, 40]. Cellular patterns are spatially disordered, and the oscillations of individual cells are spatiotemporally uncorrelated at long distance. An in-depth phase-field study [41] has shown that the oscillatory behavior of cells is linked to the stable spacing range of the cellular array (see Fig. 10 of [41]). One of the objectives of the DECLIC-DSI experiments is to create a data bank of benchmark experiments in diffusive conditions. It was then necessary to validate the physical characteristic data of the alloy for a pertinent quantitative comparison with numerical simulations. This led us for example to redetermine the solute partition coefficient of the succinonitrile-camphor alloy, focusing on the alloy concentration range used in DECLIC-DSI [42]. However, the comparison with 3D phase-field simulations evidenced some differences in primary spacings that are partly explained by the specificities of the thermal field in the 3D geometries [43, 44]. Especially, a new modeling approach was developed that couples the 3D phase-field model to a time-dependent calculation of the thermal diffusion in the adiabatic zone [44], thus accounting for latent heat release and finite heat transport [43]. The comparison with the classical approach, using frozen temperature approximation, evidenced major improvements in the agreement between the new approach of simulation and microgravity experiments for inception of morphological instability and stationary values of spacings. However, simulations still tend to underestimate the stationary spacing (see Fig. 8c of [44]).

This important study on the influence of the thermal field points out that 3D experiments introduce additional unavoidable deviations from ideal models of solidification, which are negligible or controllable in thin samples, and which affect the microstructure characteristics and dynamics. While it is well recognized that the array spacing and structure can be influenced by crystal orientation [29, 30, 45], the effects of orientation and grain boundaries remain largely unexplored in bulk samples for spatially extended arrays. The work presented here aims to explore the influence of crystalline misorientations and the presence of boundaries during large-scale bulk solidification, from both experimental and numerical points of view.

After the description of the experimental device and methods (Section 2), we start the experimental part (Section 3) with the description of the pattern and the sub-grain characterization. We show the time and spatial evolution of the primary spacing and focus on heterogeneities related to sub-boundary existence. More generally, the complexity of the primary spacing maps is completely analyzed and different mechanisms that alter the primary spacing homogeneity are described. Next, we directly compare the dynamics of primary spacing evolution in experiments and simulations (Section 4). After a brief description of the numerical methods, we analyze the simulations that correspond to bicrystals with a convergent and a divergent sub-boundaries, whose characteristics are similar to those observed in experiments. Then we show the link between the primary

spacing profile in the vicinity of sub-boundaries and the value of the average spacing in the spacing stability range. The role of the distance between the crucible border and the sub-boundary on the primary spacing profile is evidenced. Finally, conclusions are summarized in section 5.

2. Experiments

2.1 The directional solidification device DECLIC-DSI

The DSI of the DECLIC facility includes a Bridgman type furnace and the experimental cartridge [46, 47]. The Bridgman furnace is composed of a hot zone and a cold zone located at the top and bottom of the adiabatic zone, respectively, so that a temperature gradient G can be generated (between 10 and 30 K/cm). Solidification is performed by pulling the experimental cartridge containing the alloy from the hot zone towards the cold zone at a constant pulling rate V_p (between 0.1 and 30 µm/s). The experimental cartridge comprises the quartz crucible and a system of volume compensation made of stainless steel that is mandatory to accommodate the specimen volume variations associated with phase changes. The cylindrical crucible has an inner diameter of 10 mm and a length that enables about 10 cm of solidification, allowing the study of the whole development of extended 3D patterns from their initial stages up to the permanent regime of growth. The crucible is equipped with a flat glass window at the bottom and a lens immersed in the melt at the top. The main observation mode takes advantage of the complete axial transparency of the cartridge provided by these last two elements: the light coming from LEDs passes through the cartridge from the bottom to the top, crossing the interface of which the image is formed on a CCD camera; these top-view images of the microstructure are used to study array dynamics and characteristics. On the same cartridge axis, a Mach-Zehnder interferometer is also set using a He-Ne laser. The basis of the optical system is described in [48]. In the transverse observation mode, the light coming from two LEDs crosses the sample from one side to the other, which provides a real-time control of interface position and curvature (side-view image). In the current article, only images obtained by the direct axial observations are analyzed.

The organic transparent alloy used is a succinonitrile (SCN) - camphor, with a nominal concentration C_0 = 0.24 wt% camphor. The alloy was prepared with SCN purified by NASA by successive distillation and zone melting. Every step of sample preparation was carefully realized under vacuum to avoid humidity contamination. A single crystalline solid seed with a direction <100> parallel to the pulling axial direction was prepared on ground and kept unmelted during all the experimental campaigns. Further details about the experimental procedure can be found in previous works [19, 47].

Two different sets of control temperatures were used for hot and cold zones that correspond to two different thermal gradients, 19 and 12 K/cm [43]. A range of pulling velocities V_P from 0.25 to 30 µm/s was studied which covers a range of microstructures from planar to cellular to dendritic.

2.2 Description of selected experiments

In this paper, we will mainly focus on one set of experimental conditions corresponding to a thermal gradient of G = 19 K/cm and a pulling velocity of V_p = 2 µm/s. This choice is guided by the macroscopic interface shape, which is roughly flat at this velocity whereas it is convex for lower velocities and turns to concave for higher ones due to latent heat release [43]. Two different experiments were performed using these conditions: a long solidification (60 mm) at a constant pulling rate and a solidification starting at V_P = 2 µm/s and jumping to V_P = 6 µm/s after 30 mm of pulling. Both experiments have similar dynamics and we will describe here only the long solidification.

Fig. 1a shows the top-view observation of the solid-liquid interface at rest (V_P = 0, t = 0). After triggering of the pulling, we first observe a rather complex array of more or less linear ridges along sub-boundaries (Fig. 1b). The increase of visibility of sub-boundaries (SBs) is in fact induced by the boundary shape change that even occurs below the morphological instability threshold. The clearest manifestation of morphological instability is the development of a more or less uniform corrugation within the sub-grain (Fig. 1c) that defines the first visible wavelength of the instability [12]. The amplitude of all interface modulations increases and grooves start to form, but it is still difficult to identify cells (Fig. 1d). At this stage, the interface dynamics is remarkably fast and pattern disorder is high. There is then a progressive decrease of disorder and a clear pattern of cells eventually emerges (Fig. 1e). The dynamics then slows down and is associated to progressive size adjustment and array ordering (Fig. 1f).

As mentioned earlier, we started the experimental campaign with a single crystal, with a <100> direction aligned with the pulling axis as closely as possible, and only the very top of the solid seed was remelted before each new solidification experiment. But, as illustrated in Fig. 1b, numerous SBs are present and we noticed a progressive increase of sub-boundaries with the numbers of melting-solidification cycles ; we attribute the multiplication of sub-boundaries to thermomechanical stresses that lead to reorganizations of dislocations. During this first stage preceding development of morphological instability (Figs. 1a-b), the shape change of grain boundaries that leads to the observation of ridges is long known [49, 50] and has been observed for grain and sub-grain boundaries [51, 52]; however, the theoretical analysis of the behavior of sub-boundaries in this pre-instability regime is much more recent [52-54]. In this regime, SBs are far from being immobile and their motion is associated to numerous phenomena, such as merging of SBs or even nucleation of new sub-grains, which correspond to a dynamic reorganization (Fig. 2). The motion of boundaries confirms their sub-boundary nature, with low misorientation, otherwise they would be fixed [52]. Dynamic polygonisation has been studied in details in thin samples by Bottin-Rousseau et al. [52]: they also reported merging of SBs but the mechanism of formation of new SBs was different from the splitting of SBs that seems to dominate in our case. Both experimental, theoretical and numerical recent studies pointed that the mobility of SBs starts to decrease when the interface velocity approaches the onset of morphological instability, to eventually become immobile [52-54]. This behavior is confirmed in our

observations, where SBs are clearly fixed when the instability starts to develop within the sub-grains, as illustrated in Fig. 2d.

Below the morphological instability threshold, poxes presumably originating from localized crystal defects are sometimes observed within sub-grains [51, 55, 56]. Their occurrence, however, is random and not related to pulling velocity. For example, we did not observe poxes at V_P =1 µm/s and 4 µm/s; they were observed during some solidifications at 2 µm/s (inset of Fig. 1b) but not all.

During the first stages of pattern development above morphological instability (Fig. 1e), we notice that some SBs remain visible due to a particular arrangement of cells along the side of the boundaries [51, 55]. However, this visibility progressively vanishes as growth progresses; it is then difficult to locate them in the well-developed pattern (Fig. 1f). Close to the morphological instability threshold, the SBs were fixed but, comparably to what happens for dendritic patterns [57-60], the grain competition in the deep cell growth regime is dominated by mechanisms occurring close to the cell tips, including tip-splitting, elimination, and drifting. The SB can be seen as a "structure" boundary with a location and shape that depends generally on the evolution of the cellular patterns in the two adjacent grains; locating main SBs is an important issue in experimental analysis, and we will come back to this point in §3.1.

The *in* situ and real time video corresponding to the solidification experiment at V_p = 2 µm/s and G = 19 K/cm is given as supplementary material [61]. Observing this video, we notice major points that will be important for the following parts:

- cells are drifting, with a tendency to go from the image top to its bottom, even if the drifting direction varies depending on the area of the image;

- Fig. 3 gathers eliminations and tip-splittings observed in the pattern during the whole solidification after the coarsening stage (from t = 3.3 to 8.2 h). We observe numerous tip-splittings but those that lead to several stable cells (full red diamonds) are very rare: most of them are followed by the elimination of one of the cells resulting from splitting, and are considered as non-stable (empty red diamonds). Eliminations (green circles) are very numerous but not homogeneously distributed along the interface: when they are not associated to previous tip-splittings, they are mainly located along a line on the right side of the pattern.

2.3 Pattern characterization

In situ and continuous observation leads to a large number of images: combining all diagnostics, a typical solidification generates 7 to 10 thousands grey-scale images. In-house software had to be developed and validated to extract relevant quantitative data on very large image sequences, of variable homogeneity and contrast quality. It gathers several image and data-processing procedures. It was implemented in Python and makes extensive use of its open-source scientific libraries NumPy and SciPy.

Quantitative characterization of the pattern consists of measuring the evolution, as a function of time and growth parameters, of the characteristics that describe the interface

morphology, such as primary spacing, order/disorder level of the pattern, shape of structures, and tip radius. Concerning shape of structures and tip radius, measurements are based on interferometric analysis that is not described (more information in Bergeon et al. [62]) since this work is not focused on those characteristics.

The first step of the treatment on a developed pattern is to identify and label each structure (cell/dendrite). A binary mask is created where each cell is separately labeled, so that the position of the center of each cell can be calculated. Based on the image of the labeled centers of cells, a Voronoi tessellation reliably finds the first neighbors, at each instant of the solidification, so that maps of the number of first neighbors can be drawn, to get information on the quantity of topological defects in the pattern. The Voronoi tessellation is also used to calculate the primary spacing which corresponds to the average of the center-to-center distances of a cell with its first-neighbors. Each structure is tracked from one image to the following one so that its motion can be analyzed (trajectory, velocity), as well as elimination or nucleation of new structures. More details on the methods of data treatment can be found elsewhere [63].

For the first stages of development of morphological instability, while only a more or less uniform corrugation is visible, the former method cannot be applied to determine the characteristic size corresponding to the primary spacing. The earliest interface patterns are then analyzed using Fourier spectrograms of images.

An additional procedure was developed to accurately determine the location of sub-boundaries. First, for each one of the images (or a selection of images), 9 different images are created to help in the preparation of the sub-grain determination: the created images are based on the raw and squared images, the average direction of cells, the cell's velocity (average and in the x and y directions) magnitude and sign. Based on the created images, a mask can be defined where each cluster is labelled to a sub-grain. Since each cell is tracked during its entire "lifetime", the location of the sub-boundary can be followed.

3. Experimental results

3.1 Sub-grain identification and characterization

The growth direction of a cell/dendrite rotates from the thermal gradient direction at a low velocity, to the closest <100> direction as pulling rate increases [29, 30]. This implies that the growth direction will be misoriented with respect to the pulling/thermal axis if no <100> direction is perfectly aligned with this axis. If the misalignment between the preferred growth direction <100> and the pulling/thermal axis is large enough, structures are tilted with respect to the optical axis, and this can be used to distinguish sub-grains. In the cellular regime, there is no striking microstructural difference between sub-grains, since the effects of misorientation are low at low pulling velocities.

The only obvious way to identify sub-grains (SGs), and therefore sub-boundaries, is to analyze the trajectories of cells: each sub-grain is characterized by a collective drift of cells, of specific direction and amplitude, caused by its particular misalignment to the

pulling/thermal axis. The experiment at V_P = 2 µm/s falls in this category: the microstructure is not strikingly different between SGs but we notice the presence of areas characterized by different drifting velocities, and the different SGs are identified by grouping cells with similar drifting velocities.

We are able to follow each cell in time, and Fig. 4a and b show each cell's velocity magnitude and direction, respectively, after around 40 mm of solidification. Due to small misorientations, both directions and amplitudes are required to discriminate the SGs and several successive images may be used to validate the location of SBs which are freehand drawn on Fig. 4. Sub-grains are then named as indicated on Fig. 4. We see that the cells of SG 1 move in a direction of approximately -45° (measured counter-clockwise with right = 0°), while the cells in SG 2 move at -110°, which results in the two groups opposing each other: the sub-boundary 1-2 is convergent, as is the sub-boundary 3-2. The cells of the SG 3 move in almost the same direction as the cells of SG 1, but slightly faster: the sub-boundary 1-3 is divergent. The precise determination of SBs location is performed using the procedure described in §2.3, and an additional label referring to the SG belonging is given to each cell (Fig. 5) and propagated to the entire experiment. This technique enables to determine the motion of SBs. Observing Fig.4, it appears that the labelling of cells belonging to SG 2 is quite easy as their gliding direction is very different compared to the other ones. Discriminating SGs 1 and 3 is more difficult and several successive images are used to validate the location of the sub-boundary.

The amplitude of drifting velocity V_d for each sub-grain is used to evaluate the tilt angle θ_g between the growth velocity V_g and the pulling velocity V_P, as described in Fig.6 considering a macroscopic planar interface:

$$\tan\theta_g = \frac{V_d}{V_P} \qquad (1)$$

The misorientation of sub-grains is defined by the angle θ_o between the preferred <100> growth direction and G, considered parallel to V_P. The growth angle θ_g varies relatively to θ_o, and this variation depends on the Péclet number $Pe = \lambda V_P/D$, where λ is the primary spacing and D is the solute diffusion coefficient in the liquid [29-31, 64]:

$$\frac{\theta_g}{\theta_o} = 1 - \frac{1}{1+fPe^g} \qquad (2)$$

where f and g are alloy-dependent constants. In addition, two-dimensional phase-field (PF) simulations reveal that those constants have a negligible dependence on the temperature gradient [59].

To interpret the experimental results, we performed 3D PF simulations of a SCN-0.24wt% camphor alloy with V_P = 2 microns/s and G = 19 K/cm. By using the method in Refs. [41, 44], we construct a regular hexagonal array as shown in Fig. 7a, which we use as an initial condition. Then by imposing a crystallographic tilt angle θ_o, the array is induced to drift laterally under periodic boundary conditions. Here, we vary the angle θ_o between 3° and 15° with a step of 3° and the spacing λ between 70 µm and 270 µm with a step of 20 µm, which corresponded to Pe = 0.52 and 2.00, respectively. The simulation results (symbols in Fig. 7b) reveal that the ratio between a growth angle θ_g and θ_o increases monotonically

with Pe as reported previously [29-31, 59, 64]. In addition, the results show that the relationship between θ_g/θ_o and Pe depends very weakly on θ_o such that it can be fitted by the master curve given by Eq. (2) with $f = 0.67$ and $g = 1.47$ (black line in Fig. 7b).

Based on measurements of the average primary spacing λ in each sub-grain and the corresponding average drifting velocity V_d, the Péclet number $Pe = \lambda V_P/D$ and the growth angle θ_g can be evaluated using Eq. (1). The corresponding underlying crystal misorientation θ_o for each sub-grain used in PF simulations can then be evaluated using Eq. (2). For the measured values of θ_g reported in Fig.4, angles θ_o are between 2° and 3°.

3.2 Primary spacing evolution

To study the time evolution of the primary spacing λ, we group cells according to their SG, and observe their evolution separately, as in Fig. 8. The black line is the mean spacing for the entire interface. We first observe that the primary spacing presents an overshoot associated to the coarsening phase, indicating an over-elimination of cells. The primary spacing then starts to refine slowly. Such overshoot has already been reported, for example by Seetharaman et al. [7] but in their case, the refining stage is associated to numerous tip-splitting events that affect only a small fraction of the cells in our experiment (Fig.3). Moreover, when analyzing each SG separately, we see that the "green–2" SG refines quickly towards a steady-state value of $\lambda \approx 200\,\mu m$, while the two SGs separated by the divergent boundary ("red–1" and "blue–3") evolve much more slowly and remain 10% coarser. This observation clearly suggests that sub-grain boundaries have an impact on λ but the differences cannot be explained by the very low differences in crystalline misorientation between the three SG (all of the same order and very low).

In the following, we will first analyze the influence of SBs on the primary spacing evolution before proposing different elements that contribute to the overshoot in our experiments. Those analyses are based on the time-evolution of the primary spacing map that we extracted from the image sequence (Fig. 9a). In Fig. 9b, one can check the stability of the macroscopic interface shape during the whole solidification, thus confirming that the primary spacing evolution is not due to curvature evolution. Just after the overshoot (t = 1.3 h), the spacing is highly dispersed all along the interface, but we distinguish a tendency to display smaller spacings close to the crucible border and larger ones in the center. As growth progresses, dispersion progressively decreases but the central area clearly presents larger spacing than the border (t = 2.0 h) and, moreover, we notice an extended area of larger spacings that underlines the divergent sub-boundary (between SG 1 and 3). We can also notice that the convergent boundaries are slightly marked by smaller spacings. These maps then reveal that the difference of behavior between sub-grains observed in Fig. 8 is associated to the influence of the different SBs.

We endeavored first to better evidence the role of SBs on spacing. To do so, we delimited thin and long rectangular regions aligned so that the main variable within each region is distance to the corresponding SB. These regions are drawn on the left side of Fig. 10a, for t = 1.0 h (the spacing overshoot - maximum - is reached at $t = 50$ min). The corresponding "λ-

distance to SB" scatter-plots, where each data point represents a cell, and the yellow dashed lines represent the SB are given on the right side of Fig. 10a. The x-axis maps the cell's distance to the SB, with negative distances for cells in sub-grain "1–red". At this early time, λ is homogeneously dispersed, and does not obviously depend on a cell's placement on the interface. The same "λ-distance to SB" scatter-plots are then extracted for different time (Fig. 10 b to e). As previously mentioned, the dispersion decreases after the overshoot and a structuration of spacing emerges around t = 2.9 h (Fig. 10b) and soon becomes very clear, as at t = 4.4 h (Fig. 10c). Let us analyze what happens for each SB:

- **Divergent SB:** in the SG 1 (largest SG), the cells near the SB refine more slowly than the rest, so that a peak in spacing has formed along the SB. It is already visible at $t = 1.0$ h, and it progressively builds to reach a kind of stationary shape around $t = 3.5$ h, which coincides with the stabilisation of the *plateau* of primary spacing within this sub-grain (around 225 μm). On the other side of the SB, in SG 3, we also observe this peak, and a smaller spacing for cells placed farther from the SB. The overshoot was marked by an average spacing of $\lambda \cong 250$ µm. It refines down to a *plateau* value of $\lambda \cong 225$ µm. The maximum peak at the divergent SB is $\lambda \cong 275$ µm, which is even larger than the overshoot value. The divergent SB inhibits the spacing refinement towards the *plateau* value and this inhibition of refinement extends on a quite long distance inside the SG, affecting cells as far as 2 mm ($\approx$ 10 cell widths).

  The average velocity of the SB is close to the drifting velocity of SG 3. The effect of the divergent SB on the spacing can be explained by the difference of the drifting velocities between the up-stream and down-stream cells, which induces a stretching of cells. This stretching, considering the drifting velocity of the SB, mainly affects cells from the SG 1. Schematically, cells attached to the SB then have a higher velocity compared to the other cells of the sub-grain, which leads to the stretching. For most stretched cells, the stability limit associated to tip-splitting is not reached, even if it may not be far from it as we observe numerous unstable splittings in this area and a few stable ones (Fig. 3). The occurrence of tip-splitting is linked to the value of the average spacing: the closer it is to the high limit of stability, the faster it will be reached during stretching and the more splittings will occur. Local direct measurements of cell spacing associated to splittings lead to a value of stability limit $\lambda_{max} \cong$ 280 µm. This value is close to the predicted maximum limit 308 µm by PF simulation [44]. Lastly, the spreading of the stretching within each SG also contributes to limit tip-splittings.

- **Convergent SB**: the profile of spacing in the SG 1 presents the *plateau* at the average spacing ($\lambda \cong 225$ µm), followed by a quite sharp decrease at the SB that extends only one or two cell widths. On the other side of the SB, in SG 2, the sharp decrease is quite difficult to see as it is masked by the average value decrease from 250 to 200 µm. This last point will be discussed later. Numerous eliminations occur in the SB area (Fig. 3), indicating that the low stability limit is reached, and on a short distance. Based on the spacing histograms, the stability limit for elimination is estimated at $\lambda_{min} \cong 150$ µm.

We then look for the origin of the primary spacing decrease generating an overshoot as it is not associated to numerous tip-splittings in our case. In the curves of Fig. 10 as well as in the primary spacing maps of Fig. 9, we observe an area of smaller cells ($\lambda \cong 200$ µm) close to the crucible border that progressively extends. On Fig. 10e, *plateaus* of small cells are clearly visible in the red SG 1 (between x = -6 and -4 mm) and in the green SG 2 (between x = 0 and 2 mm); we see the formation of these *plateaus* going back in time in Fig. 10d and c. A close observation of the first stages of the experiment reveals that those small cells were already present at the very first stage of microstructure formation (they are visible on the spacing maps at t = 2 h shown in Fig. 9b). Small spacings may be attributed to a different dynamical selection mechanism operating in the very beginning of the solidification and probably due to a radial inhomogeneity of the thermal field. The small spacings area progressively extends and invades the core of SGs. Drifting velocity maps, in amplitude and direction, are given in Fig. 11: the drifting velocity amplitude at the border (small spacing areas), is always slightly higher than at the central area. The propagation towards the interior of the sample of a spacing front separating lower velocity cells with larger spacing in the interior region from higher velocity cells with smaller spacing, which originate from a region near the sample border induces a decrease of average spacing. The evolution of spacing profiles in Figs. 10c-e indicates that the front velocity is larger than the SB drift velocity. This can be seen by the fact that the length of the low spacing plateau near the left crucible border increases in time as measured in the reference frame of the moving SB. A qualitatively similar propagative spacing adjustment mechanism was observed previously in thin-sample directional solidification experiments with spacing inhomogeneities in the presence of sources and sinks of cells [31]. In the present experiments, this propagation of smaller spacings into larger ones can account for the average primary spacing overshoot.

The smaller spacing cells at the border display a higher velocity. Smaller spacings are associated to smaller Péclet, and, from Eq. 2, this would lead to a slight decrease of the drifting velocity, incongruent with the observation. To explain the higher velocity, we can assume the existence of a small curvature at the border due to the radial inhomogeneity that leads to the smaller cells existence [43]. The inclination of the thermal gradient leads to a higher drifting velocity (Fig. 6 in curved interface), so that a radial drifting component would be added to the crystallographic component obtained in planar front [19]. Based on the master curve of Figure 7 and the schemes of Fig. 6, we can evaluate an angle between G and V_P equal to 2° which is sufficient to increase the drifting velocity to $\cong$ 76 nm/s. Moreover, in case of concavity, two points of the interface will get closer as the growth progresses, leading to a geometrically imposed reduction of spacing [19]; this phenomenon also contributes to the average primary spacing overshoot.

4 Comparison to 3D phase-field simulations

4.1 Model, simulations, and parameters

The PF model for solidification has been developed to investigate complex microstructure dynamics [65, 66]. The quantitative PF model used here is designed for directional solidification of dilute binary alloys. The model utilizes a thin-interface asymptotic analysis

[67] to make the width of the diffuse interface W much larger than the capillarity length d_0 while remaining quantitative [67, 68]. An anti-trapping current is introduced into the model to compensate for spurious solute trapping due to a large W [69, 70]. In addition, the model neglects solute diffusion in the solid that is much slower than in the liquid.

The conventional model contains a concentration field and a phase field φ that takes constant values in solid ($\varphi = 1$) and liquid ($\varphi = -1$) and vary smoothly across the diffuse interface. In order to enhance computational efficiency, we use a non-linear preconditioned phase field ψ of $\varphi = \tanh(\psi/\sqrt{2})$, instead of using φ, which improves the numerical stability at a large grid spacing [39, 41, 71]. The model equations are solved on a cubic lattice using a finite difference implementation of spatial derivatives and a Euler explicit time stepping scheme. Additionally, we use an integer crystal index field $p(x, y, z)$ to identify different grains for a bicrystalline simulation, which takes the value $+1$ in one grain, -1 in the other grain, and 0 in the liquid. The crystal index in the liquid can be updated by neighbor indexes [59, 60]. We implement the model on massively parallel graphic processing units (GPUs) with the computer unified device architecture (CUDA) programing language. Moreover, we use the multi-GPU computation with CUDA streams and peer-to-peer communication between GPUs to improve the efficiency of large-scale simulations. Hence, a simulation using four GPUs is about 4.4 times faster than a single GPU simulation with a test grid $N_x \times N_y \times N_z = 512 \times 512 \times 512$ under the same computing environment. Additionally, performing a simulation on multi-GPUs can improve the available device memory, such that we can achieve experimentally relevant simulations at a scale of several millimeters. In this paper, PF simulations with grid size $N_x \times N_y \times N_z = 600 \times 1584 \times 300$ are typically performed on four Nvidia Tesla P100 GPUs that cannot be carried out on a single P100 GPU due to its limited device memory size (16GB).

The PF simulations have been extensively performed for a SCN-0.24 wt% camphor alloy to investigate observations during microgravity experiments, such as oscillatory dynamics of cellular arrays [39-41] and microstructure pattern selection dynamics [44]. Here, we focus on the fixed pulling velocity V_P = 2 μm/s and temperature gradient G = 19 K/cm. We use previously studied alloy parameters: the partition coefficient k = 0.07 [42], the liquidus slope m = -1.365 K/wt%, the diffusion coefficient D = 270 $\mu m^2/s$ [40, 41], and the crystalline anisotropy ε_4 = 0.011 [40, 41, 64]. The numerical parameters are chosen to be the interface thickness $W/d_0 = 140$, the grid spacing $\Delta x/W = 1.2$, and the explicit time step $\Delta t \approx 0.0035$ s. For most simulations in following sections, the domain size is $L_x \times L_y \times L_z = 1495 \times 3960 \times 760\ \mu m^3$ and the simulated time is four or eight hours, which takes approximately 21 or 42 days of computation time with four P100 GPUs. We also use the domain size $L_x \times L_y \times L_z = 1495 \times 3900 \times 520\ \mu m^3$ in section 4.2.2 to investigate a convergent sub-grain boundary with smaller array spacing. We adopt symmetric boundary conditions in the *x* and *y* directions and periodic boundary condition in the *z* direction.

In this paper, we use the classical frozen temperature approximation (FTA) in the PF model. In a recent study [44] we showed that the thermal field can be coupled with the PF model, which evolves due to latent heat rejection at the interface and thermal diffusion within an adiabatic zone. It can quantitatively predict initial transient dynamics, including initial interface dynamics, morphological instability events, and microstructure selections.

Nevertheless, the sub-grain (SG) dynamics is caused by the lateral drift of cellular arrays after the initial transient state, and the drifting dynamics around the tip region is independent of the thermal condition [59]. Hence, for the purpose of investigating the sub-boundary (SB) dynamics, it is still reasonable to perform PF simulations with the FTA.

The PF simulations start from a regular hexagonal array of cells, as shown in Fig. 13a. The regular array is prepared by symmetrical and translational operations of a single well-oriented cell [44], with a spacing 220 or 150 μm. Then cells in the regular array are divided into two SGs by two values of crystal index in the solid [60]. We impose the polar misorientation (tilt) angle θ_0 and the azimuthal misorientation (SG drifting) angle ϕ_0 into the simulation for different SGs as described in Ref. [72]. Two series of bicrystalline simulations are performed to study both the divergent SB between SG 1 and SG 3, and the convergent SB between SG 1 and SG 2. For different SGs, in order to estimate the angle θ_0, we use Eqs. (1) and (2) together with experimentally measured values of the drifting velocity V_d and the average primary spacing λ = 220 μm. As a result, we obtain (θ_0, V_d) = (2.33°, 47 nm/s), (2.67°, 54 nm/s) and (3.07°, 62 nm/s) for SG 1, 2, and 3, respectively. The angle ϕ_0 is a projection angle of the crystal orientation axis onto the y-z plane, and it is measured counter-clockwise with the normal to a SB as 0°, as shown in Fig. 13a. According to experimental measurements, those angles are ϕ_0 = -12° for SG 1 and ϕ_0 = 165° for SG 3 around a divergent SB; ϕ_0 = -37° for SG 1 and ϕ_0 = 62° for SG 2 around a convergent SB. Some videos of those numerical simulations are available in the supplementary material [61].

4.2 Results of simulations

We carried out PF simulations at experimentally relevant time and length scales to investigate the divergent SB between SG 1 and SG 3 (Sec. 4.2.1), and the convergent SB between SG 1 and SG 2 (Sec. 4.2.2). To compare simulations with experiments more easily, we fit the experimental data points of spacings and drifting velocities on individual cells in Fig. 10 to smooth curves obtained by binning and averaging the data along the distance axis. The resulting smoothed out curves are shown in Fig. 12 and summarized below.

Near a divergent SB, a peak of spacing is formed as SG 3 drifts faster than SG 1 (Fig. 12a), which has a maximum value of $\lambda \cong$ 275 μm. The peak progressively builds to reach a stationary shape. During this process, in SG 1, the spacing decreases and forms a plateau around 225 μm. This decrease comes from the invasion of smaller cells generated near the crucible wall. Meanwhile, in SG 3, the spacing decreases at a distance away from the SB. This is because cells in SG 3 drift towards the other side of the sample and are eliminated near the crucible border. Fig. 12b shows distributions of drifting velocity at different time. Within SG 1, V_d decreases from the left border to the center of the grain. Then, V_d increases continuously across the divergent SB over about a 2 mm range and reaches a higher V_d in SG 3. The higher V_d continues until cells are eliminated near the crucible border. The average velocity of the SB is about 60 nm/s, which is close to the average drifting velocity of SG 3.

Near a convergent SB, numerous eliminations of cells occur between SG 1 and SG 2. Those eliminations lead to a sharp decrease of spacing at the SB that extends only one or two cell widths (Fig. 12c). The eliminations indicate that the lower stability limit of spacing $\lambda_{min} \cong$ 150 μm is reached at the convergent SB. In SG 1, a plateau of average spacing $\lambda \cong 225$ μm is observed, which is similar to the case of a divergent SB. However, in SG 2, the sharp decrease is quite difficult to observe as it is masked by the decrease of the average spacing from 250 to 200 μm.

4.2.1 Divergent SB

We first focus on the simulation of the divergent SB between SG 1 and SG 3. As shown in Fig. 13a, the initial microstructure (t = 0 h) in the simulation is comprised of a red grain on the left with misorientation angles (θ_0, ϕ_0) = (2.33°, -12°), and a blue grain on the right with misorientation angles (θ_0, ϕ_0) = (3.07°, 165°). A divergent boundary will form as the blue grain drifts faster than the red grain towards the right of the domain. Videos are provided in supplementary material (videos 14a,1st and 2nd parts, of [61]). In both simulation and experiment, velocities of the divergent SB are around 60 nm/s, which is close to the drifting velocity of the faster SG (SG 3). The drifting velocity in the grain upstream (SG1) is slightly higher in simulation than in experiment but remains lower than in SG3.

We notice that both simulation and experimental profiles present the same main characteristics. The evolution of spacing profiles is shown in Fig. 13b, which are fitted from discrete data measured in the simulation. A peak of spacing is formed at the location of the SB. It increases with time and finally reaches about 270 μm at the end of simulation (t = 8 h). In SG 1, the spacing shows a plateau within the sub-grain, and the spacing increases toward the peak spacing. In SG 3, the spacing decreases at a distance away from the SB. Those observations are similar to the experiment shown in Fig. 12a.

There are also differences between simulation and experiment. The plateau spacing within SG 1 tends to increase in the simulation, whereas it tends to decrease in the experiment. As a result, in the former case, the width of the spacing peak increases in SG 1, whereas the width decreases at first before stabilizing in the latter case. Also, newly created cells at the left border in PF simulation have spacings larger than the average, which is also observed in previous studies [27, 31, 59], whereas in experiment, smaller cells enter the central area.

We attribute the differences between experiment and simulation to different source types, and the distance from the source (the left border) to the SB, which is denoted by D_{SB}. Accordingly, we consider PF simulations with different initial D_{SB}, whose microstructures at t = 0 h are shown in Fig. 14. We use the same crystallographic conditions as used in Fig. 13 for all cases. The evolution of spacing profiles is plotted in the second row of Fig. 14. Those profiles show a clear influence of D_{SB} on the behavior of the plateau. As D_{SB} increases (from Fig. 14 a to c), the average spacing of the plateau and the width of spacing peak decreases. Also, the effect of a source extends over a range about 1.5 mm in four hours, and a stable plateau is observed as D_{SB} increases. Namely, if D_{SB} is large enough, a source will not affect a SB, and their effects can be distinguished; otherwise, a source can influence a SB, and they can have overlapping effects on the plateau region. In the simulation, the entering cells come directly from the source, where the stretching of cells that leads to a tail instability

generates large entering cells. In the experiment, however, the border is further away, and the entering cells come from a smaller spacing region, which probably results from a radial inhomogeneity of the thermal field.

Meanwhile, since the sample size is fixed in the simulation, varying D_{SB} also changes the distance between the SB and the right border. The right border acts like a sink where cells are eliminated, and it can also affect the spacing profile [31]. If the distance between the sink and SB is reduced to a scale comparable to the diffusion length (135 μm), the peak of spacing will be largely affected by the sink due to solute diffusion.

The evolution of V_d profiles is shown in Fig. 13c (solid lines), which are fitted from discrete data measured in the simulation with initial D_{SB} = 923 μm. The V_d profiles exhibit similar shapes near the SB as experimental measurements. We also show predicted V_d profiles based on the master curve in the same figure (symbols). The predicted V_d is calculated by using Eq. (2) with f = 0.67, g = 1.47 and the fitted spacing profiles from Fig. 13b. While the measured V_d varies continuously across the SB, the predicted V_d shows a discontinuity at the SB. The reason for the discontinuity is that the misorientation angles θ_0 of two SGs are different across the SB. Meanwhile, the ratio θ_g/θ_0 increases monotonically with the spacing according to the master curve. Therefore, the predicted $V_d(\theta_g)$ would be discontinuous while the spacing varies continuously across the SB.

We may attribute the difference between the measured and predicted V_d to the phase diffusion [31], which generically relaxes spatially modulated nonequilibrium patterns towards a spatially uniform spacing [1]. This effect is negligible for a single grain when the crystal misorientation is high [31]. However, it cannot be ignored when the crystal misorientation is low and in the presence of a divergent SB. The drifting dynamics of cells near the SB are adjusted by the phase diffusion. As shown in Fig. 13c, cells in SG 1 near the SB drift faster than the prediction, while cells in SG 3 near the SB drift slower than the prediction. Here, phase diffusion tends to unify the drifting dynamics for cells in different SGs, such that the measured V_d can vary continuously across the SB.

Additionally, we note that the mechanism of cell creation can affect the drifting velocity profile close to the left boundary of SG 1. V_d tends to decrease in the simulation, whereas it tends to increase in the experiment. In the experiment, the macroscopic curvature can lead to an increased V_d as explained previously in Sec. 3.2. In the simulation, both the source and sink can slow down cell drifting as reflected by a smaller V_d in Fig. 13c.

4.2.2 Convergent SB

We performed PF simulations with two grains that are related to SG 1 and SG 2 in the experiment. The initial regular hexagonal arrays have two different spacings of λ = 220 μm and 150 μm. For both spacings, as shown in the first row of Fig. 15, the initial microstructure (t = 0 h) is comprised of a red grain on the left with misorientation angles (θ_0, ϕ_0) = (2.33°, -37°), and a green grain on the right with misorientation angles (θ_0, ϕ_0) = (2.67°, 62°). A convergent boundary will form as the blue grain and the green grain drift

towards each other. Videos are provided in supplementary material (videos 15a and 15b of [61]).

The spacing profiles are shown in the second row of Fig. 15. There are three major observations. First, in both simulations, we observe new cells selecting spacings larger than the average near the sources at the left and right borders. At a distance away from sources, the spacing decreases towards plateau values within each grain. Second, we observe the local decrease of the spacing at a certain depth, i.e., the difference between the plateau and the minimum spacing at the convergent SB. The spacing depth is 60 μm in the simulation with an initial spacing 220 μm (Fig. 15a), while the spacing depth is 30 μm in the simulation with an initial spacing 150 μm (Fig. 15b). Third, near the convergent SB, the two SGs penetrate deeply into each other during the simulation in Fig. 15a, while cells are frequently eliminated and the interpenetration is less deep during the simulation in Fig. 15b.

The experimental observations are similar to Fig. 15b, where the spacing depth is about 30 μm and cells in both SGs are frequently eliminated near the convergent SB. Despite the initial spacing 220 μm taken from the experiment, the simulation results in Fig. 15a are different from experimental observations, which may be attributed to the grain interaction mechanism. This mechanism depends on the relative location of the selected spacing in a stability range, which is far from the lower limit in the simulation of Fig. 15a while it is closer in the simulation of Fig. 15b and in the experiment. The range of stable spacing is 108-308 μm in the simulation [44], while it is 145-278 μm in the experiment according to the analysis of histograms and measurements of spacing limits for elimination and tip-splitting events. If the selected spacing is far from the lower limit, cells in one grain can penetrate into the other grain. During this penetration process, cells adjust themselves and survive within an intercellular region of the other grain. This penetration leads to the spacing adjustment, and thus affects the spacing depth which would increase with the penetration depth. However, if the selected spacing is close to the lower limit of stability, cells are eliminated soon after they enter the sub-grain boundary region (Fig. 15b top at t=4 h). Thus, there is less deep interpenetration of cells from the two grains, and hence a smaller depression in the spacing profile is observed (Fig. 15b bottom) when compared with the larger spacing case (Fig. 15a bottom). The mechanism of grain interaction explains our observations on a convergent SB in both simulation and experiment.

5 Conclusion

In this article, experiments carried out in the DECLIC Directional Solidification Insert onboard the International Space Station were analyzed. They benefited from the microgravity environment of the ISS so that transport phenomena involved during the solidification process become essentially diffusive. It enabled us to study large cylindrical samples by suppressing fluid flow and avoiding its detrimental effects on pattern homogeneity. A transparent organic alloy (succinonitrile-0.24wt% camphor), analog to

metallic systems in terms of solidification characteristics, was used to allow *in situ* and real-time observation. The interfacial growth pattern was observed from the top during the whole solidification, so that its formation and complete evolution could be observed.

In this work, we focused on cellular patterns and on the interaction of the growing patterns with the numerous sub-boundaries that are unavoidable in a large sample size. Detailed observations of the interface patterns were used to construct space-time evolution maps of cell location and primary spacing over the whole sample and during the entire duration of solidification. Furthermore, the analysis of those maps allowed us to gain novel insights into the effects of SBs on the spatiotemporal evolution of the primary spacing.

Already for the simplest case of a macroscopically flat solidification front, the spatiotemporal evolution of the primary spacing near sub-boundaries and sample borders is generally controlled by both pattern drift [29, 30] and associated sources and sinks that can induce cell creation and elimination, respectively. We observed in both experiments and simulations that divergent and convergent sub-boundaries have strikingly different effects on this evolution. Divergent boundaries with small misorientations have cell tips from neighboring grains that move slowly away from each other for long duration, thereby generating a slow increase of spacing without cell creation (up to 20% of the maximum local increase). In contrast, convergent sub-boundaries decrease the primary spacing by cell elimination. Interestingly, the spacing maximum at divergent sub-boundaries is relatively broad (extending over relatively long distances of the order of 10 cell widths) while the spacing minimum near convergent sub-boundaries is narrower. This difference can be attributed to the fact that the primary spacing in the sub-grains away from sub-boundaries is generically closer to the lower limit of stable spacing.

The role of the average spacing value on the peak/depression amplitude is confirmed by the 3D phase-field simulations. They reveal that the spacing minimum near convergent sub-boundaries is only narrow if the primary spacing is chosen close to the lower limit of stable spacing. In contrast, if the average spacing is larger and thus farther from this stability limit, the two grain structures can interpenetrate each other without cell elimination, thereby influencing the array spacing over larger distances and broadening the minimum. The fact that, experimentally, grains were not observed to interpenetrate at the convergent sub-grain boundary investigated in the present work, while they were observed to interpenetrate in the simulations with a comparable average spacing, suggests that the lower spacing limit of array stability is larger in the experiments than in the simulations as noted in previous studies [44]. While the origin of this difference remains to be elucidated, it should not distract from the fact that experiments and simulations show consistent behavior at convergent sub-boundaries for average spacings close to the lower limit of stability.

Both experiments and phase-field simulations also reveal that, on a larger sample scale, the spacing evolution can be influenced by other spacing adjustment mechanisms operating near sample borders. In phase-field simulations, the predominant mechanisms include sources and sinks of cells at border walls that are upstream and downstream from drifting sub-grains, respectively. In experiments, in addition to those mechanisms, curvature effects near sample borders also modify the spacing profile. Importantly, in both phase-field simulations and experiments, if sources or sinks are sufficiently far from sub-boundaries, the spacing distribution exhibit a spacing plateau in between border walls and sub-boundaries. Whereas if the source or sink and the sub-boundary are too close to each other,

this plateau shrinks and can even vanish, giving rise to monotonous or non-monotonous modulations of spacing over the entire sample. Interestingly, experimental observations suggest that shrinking of this plateau can be caused by a spacing front propagation mechanism analogous to the one observed previously in thin sample directional solidification experiments [31] but the quantitative characterization of this propagation warrants further study.

The microgravity experiments provided a unique opportunity to observe for the first time the formation and evolution of directionally solidified 2D extended arrays in diffusive transport conditions. In this diffusive regime, the concentration along the interface is homogeneous so that it is possible to study those fine effects and to identify mechanisms that hinder the relaxation of the array structure to a uniform spacing. 3D experiments introduce additional unavoidable deviations from ideal models of solidification, which are negligible or controllable in thin samples, and which affect the microstructure characteristics and dynamics. Understanding the influence of each of these elements is a promising challenge, which will allow us to address unique phenomena that arise during large-scale bulk solidification, from both experimental and numerical points of view.

Acknowlegments

This work was supported by CNES (French Space Agency) and by NASA (National Aeronautics and Space Administration) Grants No. NNX12AK54G and 80NSSC19K0135. It is based on observations with the DECLIC-DSI (Directional Solidification Insert of the DEvice for the study of Critical LIquids and Crystallization) embarked on the ISS (International Space Station). Y. Song is partially sponsored by the Post Doc Investment program of Oak Ridge National Laboratory, managed by UT-Battelle, LLC.

References

[1] M.C. Cross, P.C. Hohenberg, Pattern formation outside of equilibrium, Reviews of Modern Physics 65(3) (1993) 851-1112.
[2] W. Kurz, D.J. Fisher, Dendrite Growth at the Limit of Stability - Tip Radius and Spacing, Acta Metall. 29(1) (1981) 11-20.
[3] K. Somboonsuk, J.T. Mason, R. Trivedi, Interdendritic Spacing .1. Experimental Studies, Metallurgical Transactions a-Physical Metallurgy and Materials Science 15(6) (1984) 967-975.
[4] K. Somboonsuk, R. Trivedi, Dynamical studies of dendritic growth, Acta Metall. 33(6) (1985) 1051-1060.
[5] R. Trivedi, K. Somboonsuk, Pattern-Formation during the Directional Solidification of Binary-Systems, Acta Metall. 33(6) (1985) 1061-1068.
[6] M.A. Eshelman, V. Seetharaman, R. Trivedi, Cellular spacings—I. Steady-state growth, Acta Metall. 36(4) (1988) 1165-1174.
[7] V. Seetharaman, M.A. Eshelman, R. Trivedi, Cellular spacings—II. Dynamical studies, Acta Metall. 36(4) (1988) 1175-1185.

[8] S.H. Han, R. Trivedi, Primary Spacing Selection in Directionally Solidified Alloys, Acta Metallurgica Et Materialia 42(1) (1994) 25-41.
[9] G. Hansen, S. Liu, S.Z. Lu, A. Hellawell, Dendritic array growth in the systems NH4Cl-H2O and [CH2CN](2)-H2O: steady state measurements and analysis, J. Cryst. Growth 234(4) (2002) 731-739.
[10] J.D. Hunt, Solidification and casting of metals, london, 1979.
[11] R. Trivedi, Interdendritic Spacing .2. A Comparison of Theory and Experiment, Metallurgical Transactions a-Physical Metallurgy and Materials Science 15(6) (1984) 977-982.
[12] J.A. Warren, J.S. Langer, Prediction of Dendritic Spacings in a Directional-Solidification Experiment, Phys. Rev. E 47(4) (1993) 2702-2712.
[13] J.D. Hunt, S.Z. Lu, Numerical modeling of cellular/dendritic array growth: spacing and structure predictions, MMTA 27(3) (1996) 611-623.
[14] G.L. Ding, W.D. Huang, X. Huang, X. Lin, Y.H. Zhou, On primary dendritic spacing during unidirectional solidification, Acta Mater. 44(9) (1996) 3705-3709.
[15] H. Chen, Y.S. Chen, X. Wu, S.N. Tewari, History dependence of primary dendrite spacing during directional solidification of binary metallic alloys and interdendritic convection, J. Cryst. Growth 253(1-4) (2003) 413-423.
[16] S. Gurevich, M. Amoorezaei, N. Provatas, Phase-field study of spacing evolution during transient growth, Phys. Rev. E 82(5) (2010).
[17] S. Gurevich, A. Karma, M. Plapp, R. Trivedi, Phase-field study of three-dimensional steady-state growth shapes in directional solidification, Phys. Rev. E 81(1) (2010) 011603
[18] S. Bottin-Rousseau, A. Pocheau, Self-organized dynamics on a curved growth interface, Phys. Rev. Lett. 87(7) (2001) 076101.
[19] C. Weiss, N. Bergeon, N. Mangelinck-Noel, B. Billia, Cellular pattern dynamics on a concave interface in three-dimensional alloy solidification, Phys. Rev. E 79(1) (2009) 011605.
[20] B. Drevet, H. Nguyen Thi, D. Camel, B. Billia, M.D. Dupouy, Solidification of aluminium–lithium alloys near the cell/dendrite transition-influence of solutal convection, J. Cryst. Growth 218(2) (2000) 419-433.
[21] H. Jamgotchian, N. Bergeon, D. Benielli, P. Voge, B. Billia, R. Guerin, Localized microstructures induced by fluid flow in directional solidification, Phys. Rev. Lett. 87(16) (2001) 166105.
[22] R. Trivedi, S. Liu, P. Mazumder, E. Simsek, Microstructure development in the directionally solidified Al-4.0 wt% Cu alloy system, Sci Technol Adv Mat 2(1) (2001) 309-320.
[23] H.N. Thi, Y. Dabo, B. Drevet, M.D. Dupouy, D. Camel, B. Billia, J.D. Hunt, A. Chilton, Directional solidification of Al-1.5 wt% Ni alloys under diffusion transport in space and fluid-flow localisation on earth, J. Cryst. Growth 281(2-4) (2005) 654-668.
[24] F.L. Mota, Y. Song, J. Pereda, B. Billia, D. Tourret, J.-M. Debierre, R. Trivedi, A. Karma, N. Bergeon, Convection Effects During Bulk Transparent Alloy Solidification in DECLIC-DSI and Phase-Field Simulations in Diffusive Conditions, Jom 69(8) (2017) 1280-1288.
[25] R.N. Grugel, Y. Zhou, Primary Dendrite Spacing and the Effect of Off-Axis Heat-Flow, Metallurgical Transactions a-Physical Metallurgy and Materials Science 20(5) (1989) 969-973.

[26] R. Trivedi, V. Seetharaman, M.A. Eshelman, The Effects of Interface Kinetics Anisotropy on the Growth Direction of Cellular Microstructures, Metallurgical Transactions a-Physical Metallurgy and Materials Science 22(2) (1991) 585-593.
[27] A.G. Borisov, O.P. Fedorov, V.V. Maslov, Growth of succinonitrile dendrites in different crystallographic directions, J. Cryst. Growth 112(2) (1991) 463-466.
[28] C.A. Gandin, M. Eshelman, R. Trivedi, Orientation dependence of primary dendrite spacing, Metallurgical and Materials Transactions a-Physical Metallurgy and Materials Science 27(9) (1996) 2727-2739.
[29] S. Akamatsu, T. Ihle, Similarity law for the tilt angle of dendrites in directional solidification of non-axially-oriented crystals, Phys. Rev. E 56(4) (1997) 4479-4485.
[30] J. Deschamps, M. Georgelin, A. Pocheau, Growth directions of microstructures in directional solidification of crystalline materials, Phys. Rev. E 78(1) (2008) 011605.
[31] Y. Song, S. Akamatsu, S. Bottin-Rousseau, A. Karma, Propagative selection of tilted array patterns in directional solidification, Phys Rev Mater 2(5) (2018).
[32] K.A. Jackson, J.D. Hunt, Transparent compounds that freeze like metals, Acta Metall. 13(11) (1965) 1212-1215.
[33] S. Akamatsu, G. Faivre, T. Ihle, Symmetry-broken double fingers and seaweed patterns in thin-film directional solidification of a nonfaceted cubic crystal, Phys. Rev. E 51(5) (1995) 4751-4773.
[34] M. Georgelin, A. Pocheau, Oscillatory instability, limit cycle, and transition to doublets in directional solidification, Phys. Rev. Lett. 79(14) (1997) 2698-2701.
[35] B. Billia, H. Jamgotchian, H.N. Thi, Influence of sample thickness on cellular branches and cell-dendrite transition in directional solidification of binary alloys, J. Cryst. Growth 167(1–2) (1996) 265-276.
[36] N. Bergeon, R. Trivedi, B. Billia, B. Echebarria, A. Karma, S. Liu, C. Weiss, N. Mangelinck, Necessity of investigating microstructure formation during directional solidification of transparent alloys in 3D, Advances in Space Research 36(1) (2005) 80-85.
[37] A. Bogno, H. Nguyen-Thi, A. Buffet, G. Reinhart, B. Billia, N. Mangelinck-Noel, N. Bergeon, J. Baruchel, T. Schenk, Analysis by synchrotron X-ray radiography of convection effects on the dynamic evolution of the solid-liquid interface and on solute distribution during the initial transient of solidification, Acta Mater. 59(11) (2011) 4356-4365.
[38] G. Reinhart, C.A. Gandin, N. Mangelinck-Noël, H. Nguyen-Thi, J.E. Spinelli, J. Baruchel, B. Billia, Influence of natural convection during upward directional solidification: A comparison between in situ X-ray radiography and direct simulation of the grain structure, Acta Mater. 61(13) (2013) 4765-4777.
[39] N. Bergeon, D. Tourret, L. Chen, J.-M. Debierre, R. Guerin, A. Ramirez, B. Billia, A. Karma, R. Trivedi, Spatiotemporal Dynamics of Oscillatory Cellular Patterns in Three-Dimensional Directional Solidification, Phys. Rev. Lett. 110(22) (2013).
[40] J. Pereda, F.L. Mota, L. Chen, B. Billia, D. Tourret, Y. Song, J.-M. Debierre, R. Guerin, A. Karma, R. Trivedi, N. Bergeon, Experimental observation of oscillatory cellular patterns in three-dimensional directional solidification, Phys. Rev. E 95(1) (2017) 012803.
[41] D. Tourret, J.-M. Debierre, Y. Song, F.L. Mota, N. Bergeon, R. Guerin, R. Trivedi, B. Billia, A. Karma, Oscillatory cellular patterns in three-dimensional directional solidification, Phys. Rev. E 92(4) (2015) 042401.

[42] F.L. Mota, L.M. Fabietti, N. Bergeon, L.L. Strutzenberg, A. Karma, B. Billia, R. Trivedi, Quantitative determination of the solidus line in the dilute limit of succinonitrile-camphor alloys, J. Cryst. Growth 447 (2016) 31-35.
[43] F.L. Mota, N. Bergeon, D. Tourret, A. Karm, R. Trivedi, B. Billia, Initial transient behavior in directional solidification of a bulk transparent model alloy in a cylinder, Acta Mater. 85 (2015) 362-377.
[44] Y. Song, D. Tourret, F.L. Mota, J. Pereda, B. Billia, N. Bergeon, R. Trivedi, A. Karma, Thermal-field effects on interface dynamics and microstructure selection during alloy directional solidification, Acta Mater. 150 (2018) 139-152.
[45] S. Akamatsu, G. Faivre, Anisotropy-driven dynamics of cellular fronts in directional solidification in thin samples, Phys. Rev. E 58(3) (1998) 3302-3315.
[46] G. Pont, S. Barde, B. Zappoli, F. Duclos, Y. Garrabos, C. Lecoutre, D. Beysens, B. Billia, N. Bergeon, N. Mangelinck, R. Marcout, D. Blonde, DECLIC: a facility to study crystallization and critical fluids, 60th International Astronautical Congress, Daejeon, Republic of Korea, 2009.
[47] N. Bergeon, A. Ramirez, L. Chen, B. Billia, J. Gu, R. Trivedi, Dynamics of interface pattern formation in 3D alloy solidification: first results from experiments in the DECLIC directional solidification insert on the International Space Station, Journal of Materials Science 46(19) (2011) 6191-6202.
[48] H. Jamgotchian, N. Bergeon, D. Benielli, P. Voge, B. Billia, In situ observation and interferometric characterization of solid-liquid interface morphology in directionally growing transparent model systems, Journal of Microscopy-Oxford 203 (2001) 119-127.
[49] S.R. Coriell, R.F. Sekerka, Morphological stability near a grain boundary groove in a solid-liquid interface during solidification of a pure substance, J. Cryst. Growth 19(2) (1973) 90-104.
[50] S.R. Coriell, R.F. Sekerya, Morphological stability near a grain boundary groove in a solid-liquid interface during solidification of a binary alloy, J. Cryst. Growth 19(4) (1973) 285-293.
[51] N. Noel, H. Jamgotchian, B. Billia, Influence of grain boundaries and natural convection on microstructure formation in cellular directional solidification of dilute succinonitrile alloys in a cylinder, J. Cryst. Growth 187(3-4) (1998) 516-526.
[52] S. Bottin-Rousseau, S. Akamatsu, G. Faivre, Dynamical polygonization below the cellular-bifurcation threshold in thin-sample directional solidification, Physical Review B 66(5) (2002).
[53] G. Faivre, S. Bottin-Rousseau, S. Akamatsu, The trajectory of subboundary grooves during directional solidification of dilute alloys, Comptes Rendus Physique 14(2) (2013) 149-155.
[54] S. Ghosh, A. Karma, M. Plapp, S. Akamatsu, S. Bottin-Rousseau, G. Faivre, Influence of morphological instability on grain boundary trajectory during directional solidification, Acta Mater. (2019).
[55] R.J. Schaefer, M.E. Glicksman, Initiation of dendrites by crystal imperfections, Metall. Trans. 1(7) (1970) 1973-1978.
[56] N. Noel, H. Jamgotchian, B. Billia, In situ and real-time observation of the formation and dynamics of a cellular interface in a succinonitrile-0.5 wt% acetone alloy directionally solidified in a cylinder, J. Cryst. Growth 181(1-2) (1997) 117-132.

[57] N. D'Souza, M.G. Ardakani, A. Wagner, B.A. Shollock, M. McLean, Morphological aspects of competitive grain growth during directional solidification of a nickel-base superalloy, CMSX4, Journal of Materials Science 37(3) (2002) 481-487.
[58] A. Wagner, B.A. Shollock, M. McLean, Grain structure development in directional solidification of nickel-base superalloys, Materials Science and Engineering: A 374(1–2) (2004) 270-279.
[59] D. Tourret, A. Karma, Growth competition of columnar dendritic grains: A phase-field study, Acta Mater. 82(0) (2015) 64-83.
[60] D. Tourret, Y. Song, A.J. Clarke, A. Karma, Grain growth competition during thin-sample directional solidification of dendritic microstructures: A phase-field study, Acta Mater. 122 (2017) 220-235.
[61] See Supplementary Material at [URL will be inserted by publisher] for video of experiment (Video 1 _ Pulling rate = 2 μm/s ; thermal gradient = 19 K/cm ; Succinonitrile – 0.24 wt% Camphor) and videos of 3D Phase-field (Video 14a_1st part : Divergent SB t = 0 to 4 hours and Video 14a_2nd part: Divergent SB t = 4 to 8 hours. Initial spacing 220 micron ; Video 15a: Convergent SB with an initial spacing 220 μm ; Video 15b : Convergent SB with an initial spacing 150 μm).
[62] N. Bergeon, C. Weiss, N. Mangelinck-Noel, B. Billia, Interferometric method for the analysis of dendrite growth and shape in 3D extended patterns in transparent alloys, Trans. IIM 62(4-5) (2009) 455-460.
[63] J. Pereda, Y. Song, F.L. Mota, B. Billia, J.-M. Debierre, R. Guerin, A. Karma, R. Trivedi, N. Bergeon, Primary spacing evolution during microstructure formation in 3D directional solidification: methods of data treatment of microgravity experiments conducted in the DECLIC-DSI, 67th International Astronautical Congress, Guadalajara, Mexico, 2016.
[64] J. Ghmadh, J.-M. Debierre, J. Deschamps, M. Georgelin, R. Guérin, A. Pocheau, Directional solidification of inclined structures in thin samples, Acta Mater. 74 (2014) 255-267.
[65] W.J. Boettinger, J.A. Warren, C. Beckermann, A. Karma, Phase-field simulation of solidification, Annual Review of Materials Research 32 (2002) 163-194.
[66] I. Steinbach, Why Solidification? Why Phase-Field?, JOM 65(9) (2013) 1096-1102.
[67] A. Karma, W.J. Rappel, Quantitative phase-field modeling of dendritic growth in two and three dimensions, Physical Review E 57(4) (1998) 4323-4349.
[68] A. Karma, W.J. Rappel, Phase-field method for computationally efficient modeling of solidification with arbitrary interface kinetics, Physical Review E 53(4) (1996) 3017.
[69] A. Karma, Phase-field formulation for quantitative modeling of alloy solidification, Physical Review Letters 87(11) (2001) 115701.
[70] B. Echebarria, R. Folch, A. Karma, M. Plapp, Quantitative phase-field model of alloy solidification, Physical Review E 70(6) (2004) 1604.
[71] K. Glasner, Nonlinear Preconditioning for Diffuse Interfaces, Journal of Computational Physics 174(2) (2001) 695-711.
[72] Y. Song, Theoretical modeling of cellular and dendritic solidification microstructures, Northeastern University, 2017.

Figure(s)

FIGURE 1

Figure 1: Sequence of formation of the interface microstructure (SCN–0.24 wt % camphor, $V_p = 2\,\mu m/s$, G=19 K/cm). t denotes the solidification time elapsed, and L the solidification length ($L = V_p \times t$) attained. Video is provided in supplementary material (video1 of [61]).

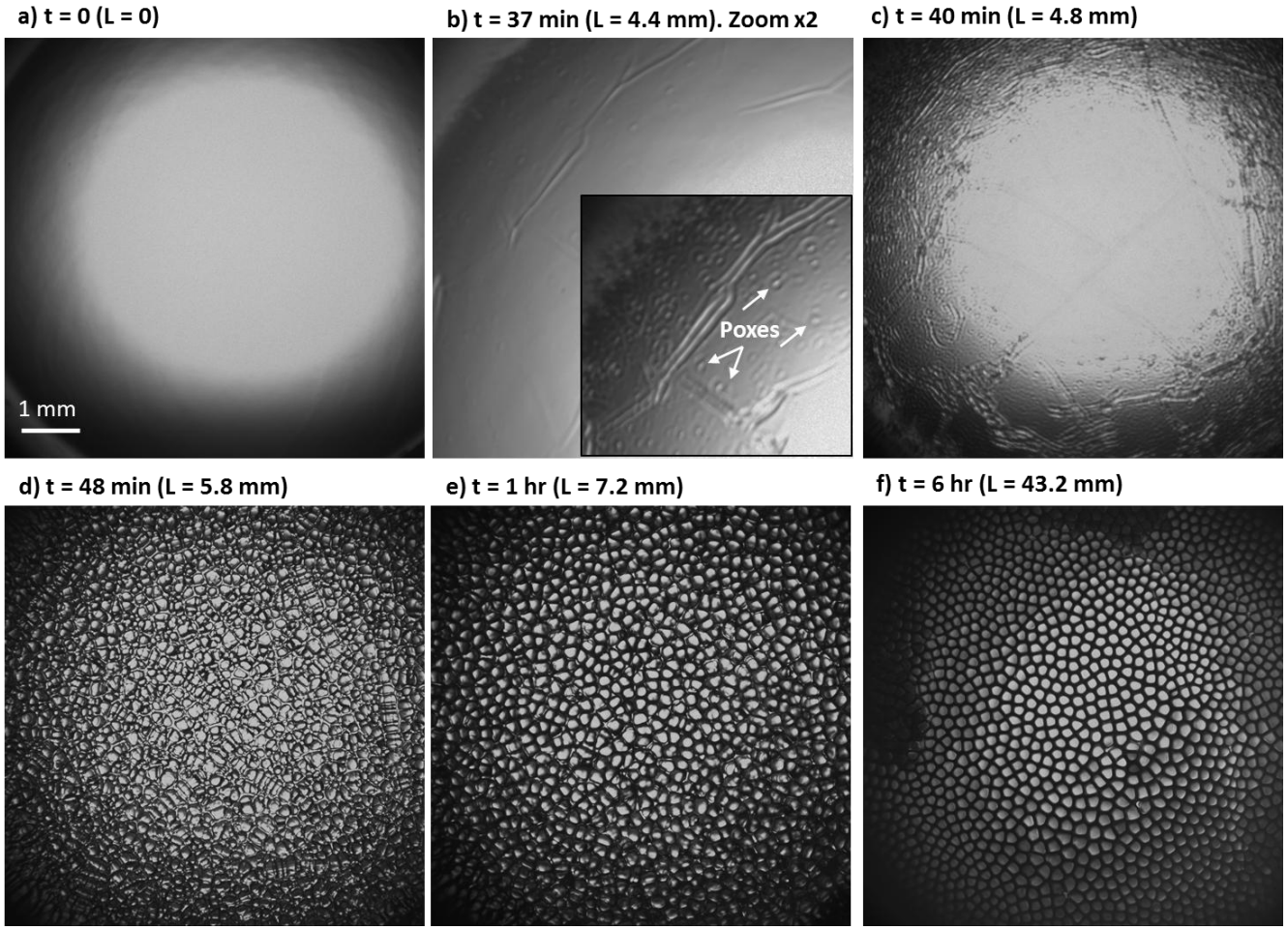

Figure(s)

FIGURE 2

Figure 2: Top-view images of the interface during the initial transient, preceding morphological instability. a) Interface area presenting both nucleation and elimination of sub-grains. b) Sequence of a SG nucleation c) Sequence of sub-grains eliminations. d) Motion of SBs. The white arrows in i show the direction of movement of the boundaries. The yellow dashed lines in ii, iii, and iv show the position of the sub-grain boundaries in i, ii, and iii respectively. The red arrow in iv shows a boundary that kept moving even after all the other boundaries have stopped. (SCN–0.24 wt % camphor, $V_p = 1\,\mu m/s$, G=19 K/cm)

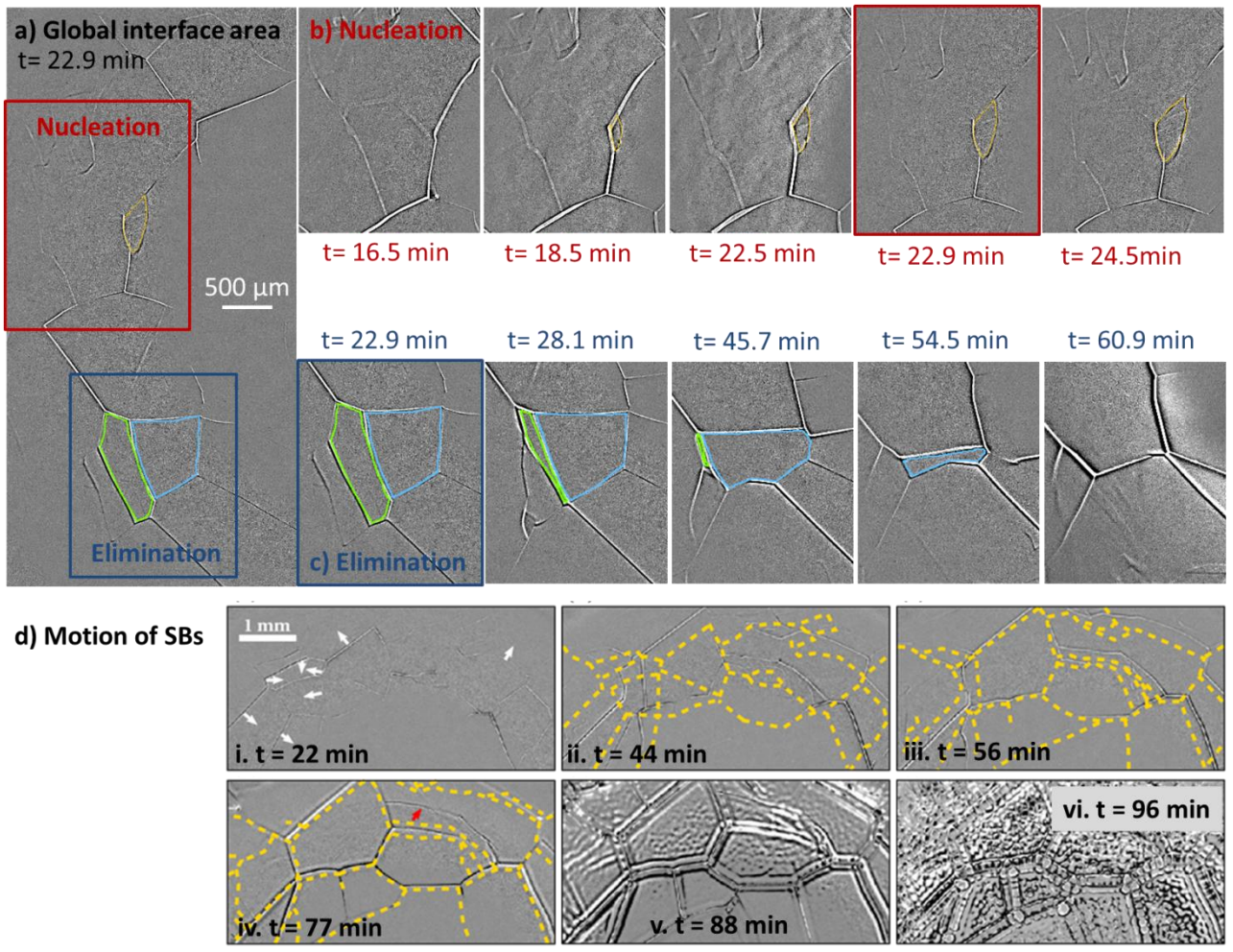

Figure(s)

FIGURE 3

Figure 3 : Eliminations (●), stable (♦) and unstable (◊) tip-splittings during the solidification duration, after the coarsening stage (from t = 3.3 to 8.2 h). (SCN–0.24 wt % camphor, $V_p = 2\,\mu m/s$, G=19 K/cm)

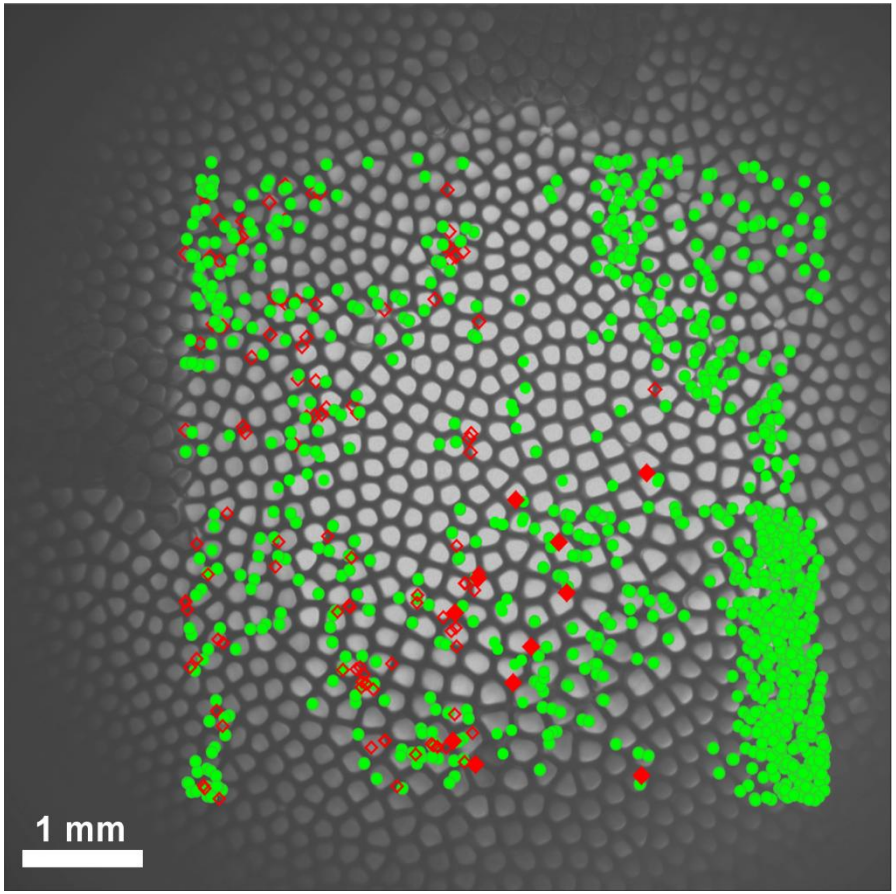

Figure(s)

FIGURE 4

Figure 4: Analysis of cell-drift to identify sub-grains: a) apparent velocity, and b) apparent direction, after pulling $42.4\ mm$ *(SCN–0.24 wt % camphor,* $V_p = 2\ \mu m/s$*, G=19 K/cm)*

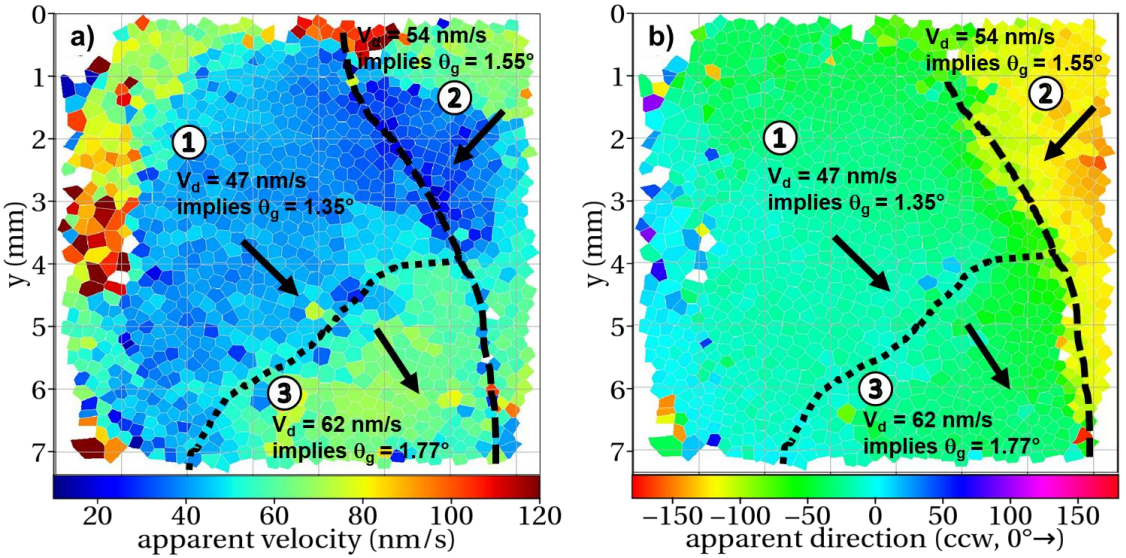

Figure(s)

FIGURE 5

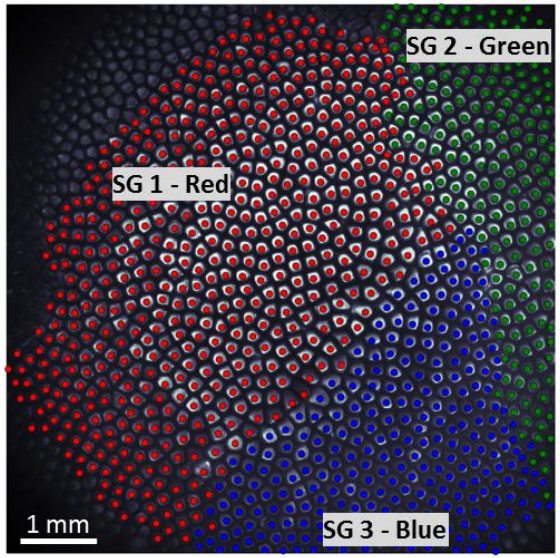

Figure 5: Cells labelled according to sub-grain determination. (SCN–0.24 wt % camphor, $V_p = 2\,\mu m/s$, G=19 K/cm)

Figure(s)

FIGURE 6

Figure 6: Scheme of the different relevant directions and angles, illustrated on a curved interface. V_P: pulling velocity ; V_g : growth velocity ; V_d : drift velocity of cell tip in the observation plane. θ_g: tilt angle between V_g and V_p; θ_o: misorientation angle, between the preferred <100> growth direction and V_g. θ_{o_Plan} is the reference misorientation angle defined when the interface is plane, which means that G is aligned with V_P.

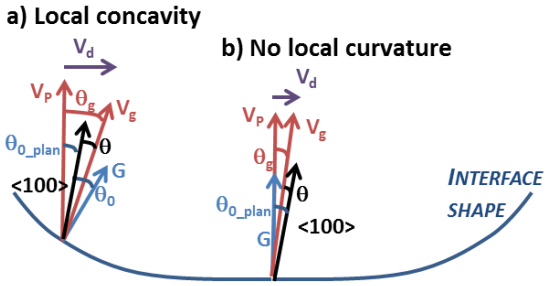

Figure(s)

FIGURE 7

Figure 7: The drift dynamics of a hexagonal array. Phase-field simulations with a SCN-0.24wt% camphor alloy are performed at V_p = 2 μm/s and G = 19 K/cm. By introducing a tilt angle θ_0, a regularly ordered hexagonal array with the spacing λ (a) drifts laterally under periodic boundary conditions. Symbols in (b) show the simulation results of the growth angle θ_g scaled by θ_0 as a function of $Pe = \lambda V_p/D$. We consider different angles of θ_0: 3° (blue circle), 6 °(red up-pointing triangle), 9 ° (blue down-pointing triangle), 12 ° (purple square), and 15° (green diamond). The black curve is the fitting equation with constants f = 0.67 and g = 1.47.

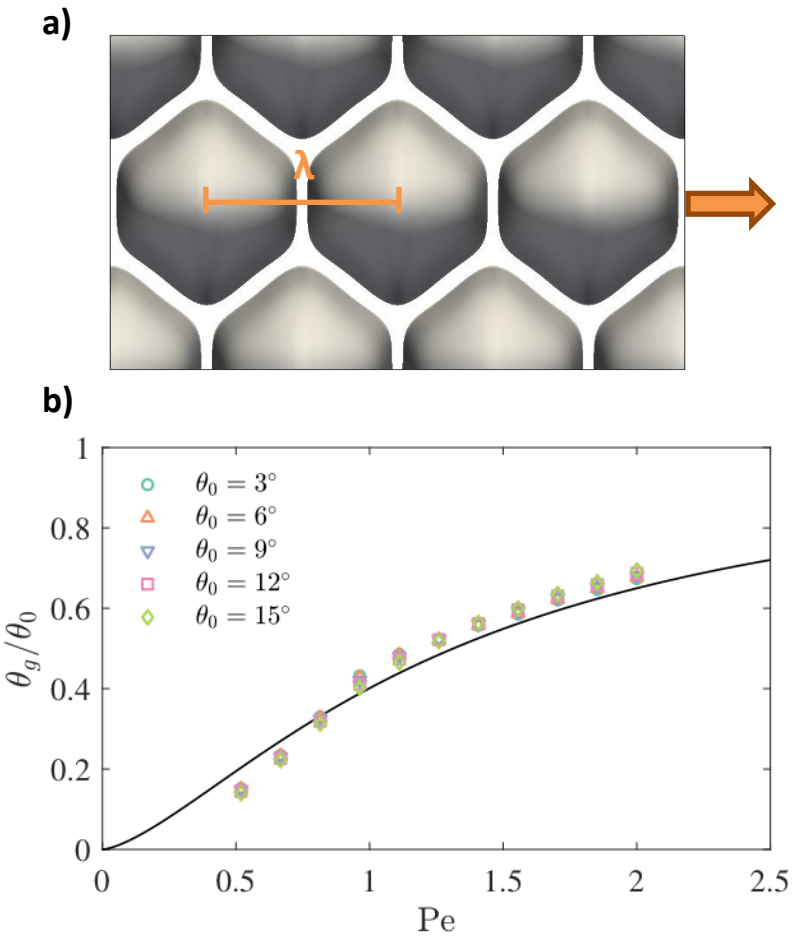

Figure(s)

FIGURE 8

Figure 8: Primary spacing evolution: average on the whole interface and by sub-grain. (SCN–0.24 wt % camphor, $V_p = 2\ \mu m/s$, G=19 K/cm)

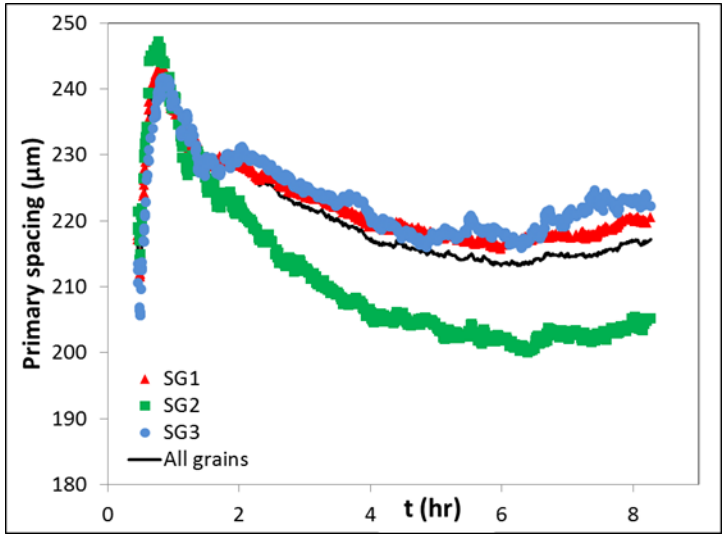

Figure(s)

FIGURE 10

Figure 10: Time evolution of scatter-plots of primary spacing as a function of distance from each SB for the regions defined in a. (SCN–0.24 wt % camphor, V_p=2 µm/s G=19 K/cm)

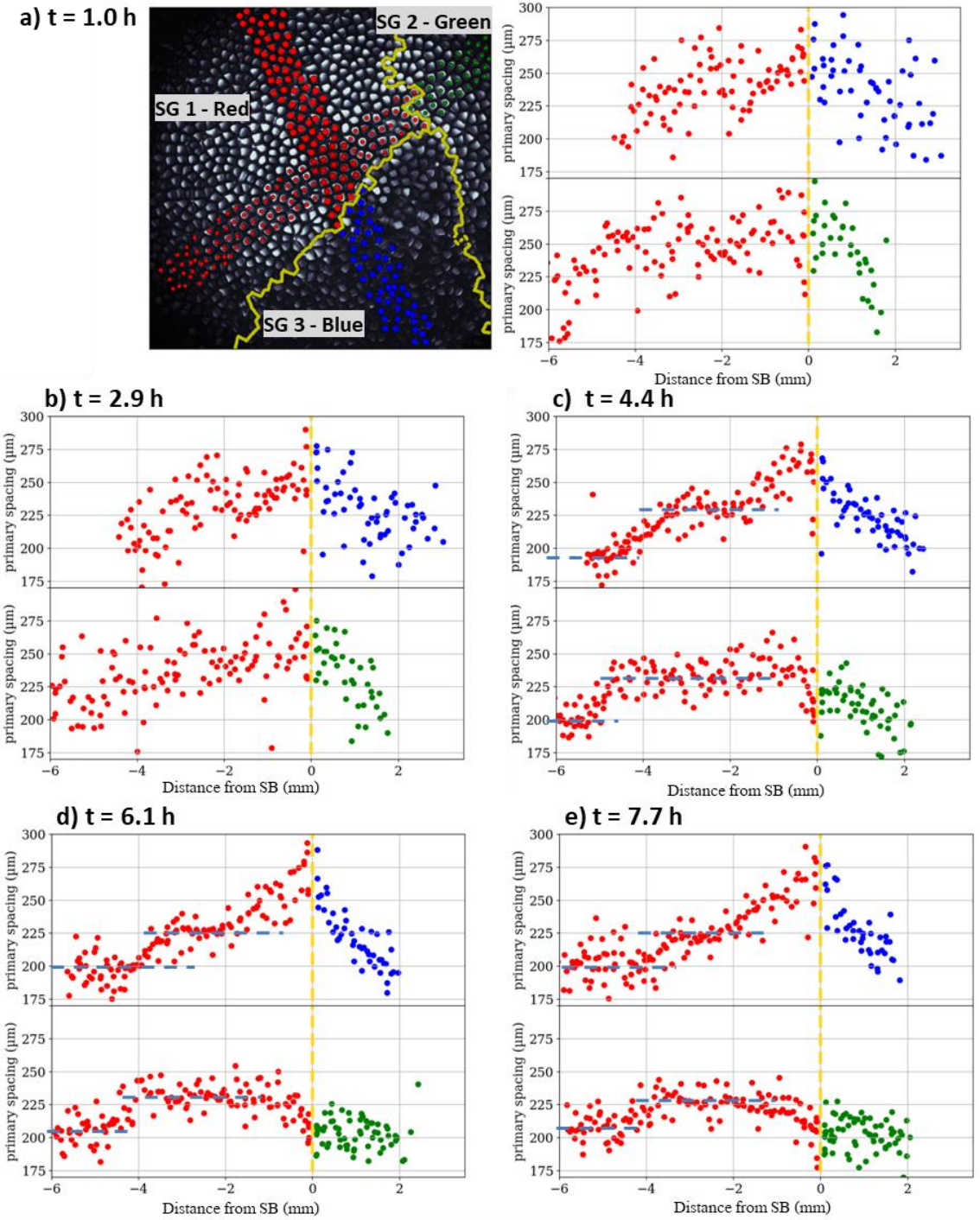

Figure(s)

FIGURE 11

Figure 11: a) Primary spacing, b) drifting direction, and c) amplitude maps at t=6.6h. Blue bold lines correspond to SBs, and yellow rectangles to areas of spacing analysis of Figure 10. Dashed lines in a) and c) mark the limits of large variations of the represented parameter. (SCN–0.24 wt % camphor, V_p=2 µm/s, G=19 K/cm)

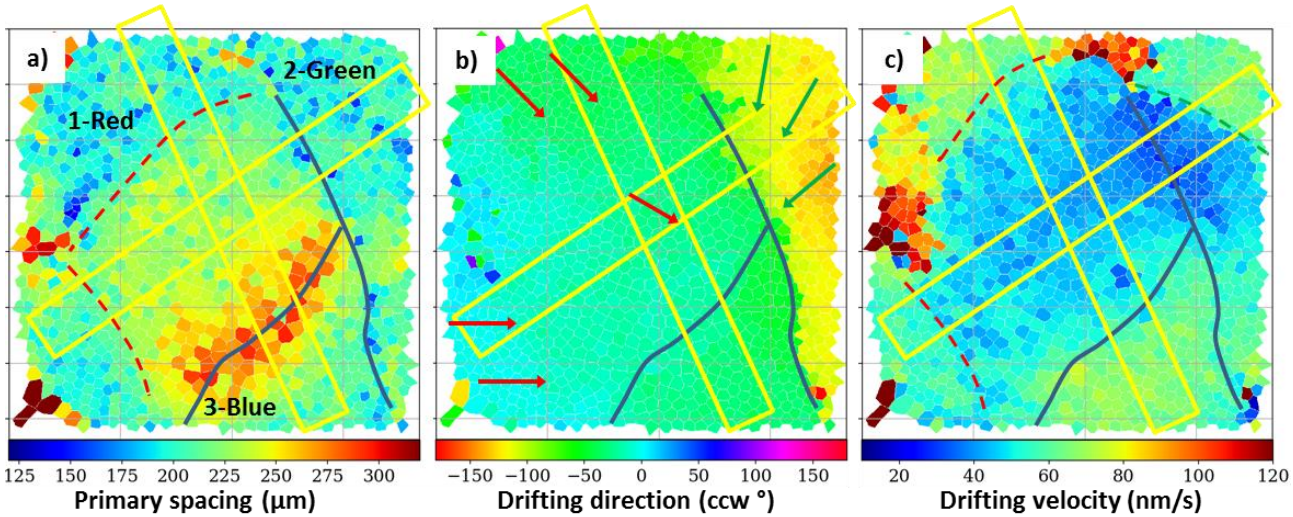

Figure(s)

FIGURE 12

Figure 12: Experimental measurements of spacing profile and drift velocity around the SBs. We measure the time evolutions of spacing profiles (a) - (b) and the drift velocities (c)-(d) around the SBs as a function of distance from a SB in Figure 10. The left and the right columns are for the results around the divergent and convergent SBs, respectively.

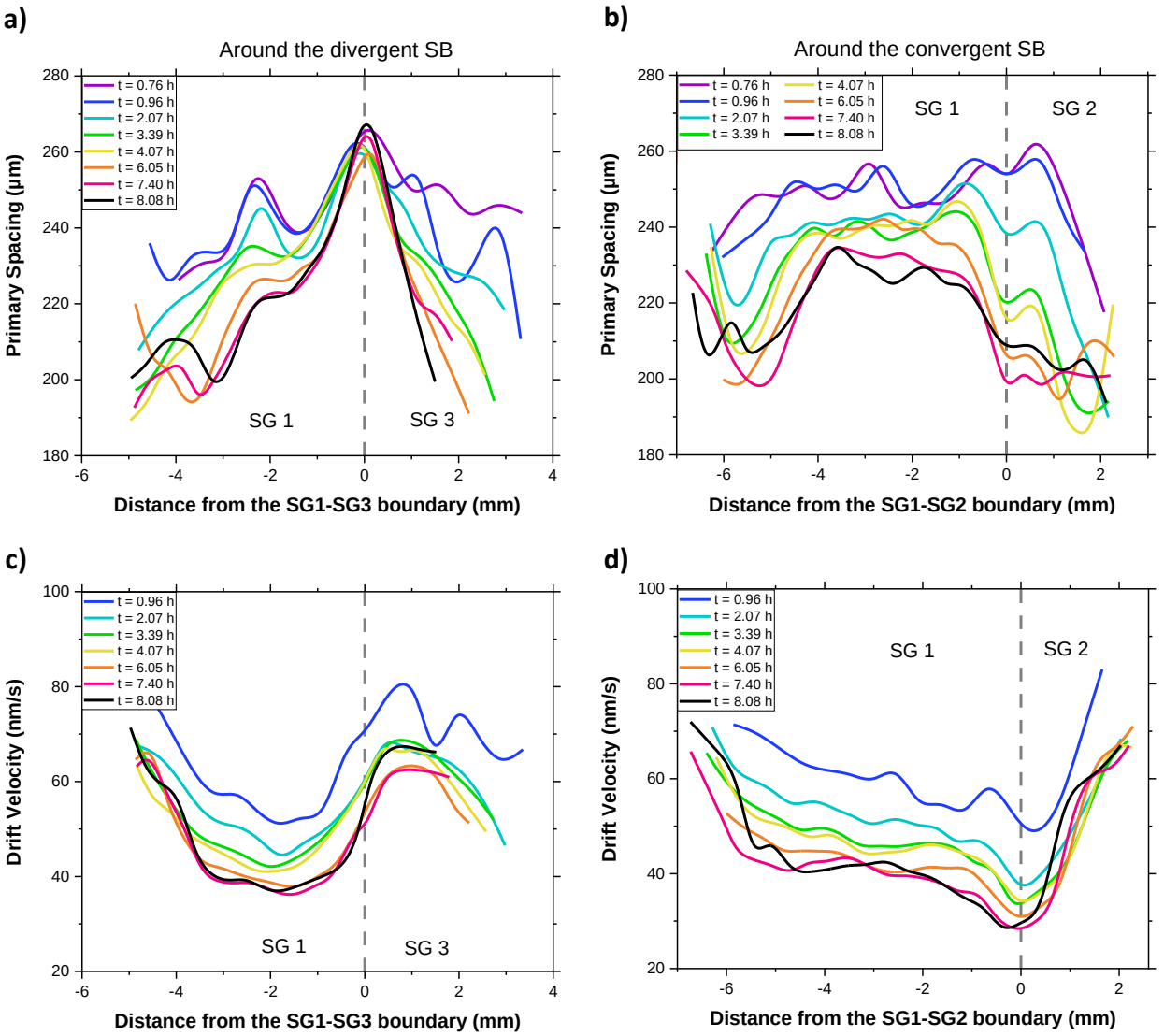

Figure(s)

FIGURE 13

Figure 13: Phase-field simulation of the divergent SB between SG 1 (left red grain) and SG 3 (right blue grain). a) Microstructures seen from the top of the interface at t=0 h, t=4 h and t=8 h. The colored arrow with the solid line indicates the drifting direction for each SG. b) Evolution of spacing profiles. c) Evolution of measured V_d profiles (solid lines) and the predicted V_d profiles (symbols). The predicted V_d is calculated by using Eq. (2) with f = 0.67, g = 1.47 and the spacing profiles in (b). The black dashed lines indicate the location of the SB.

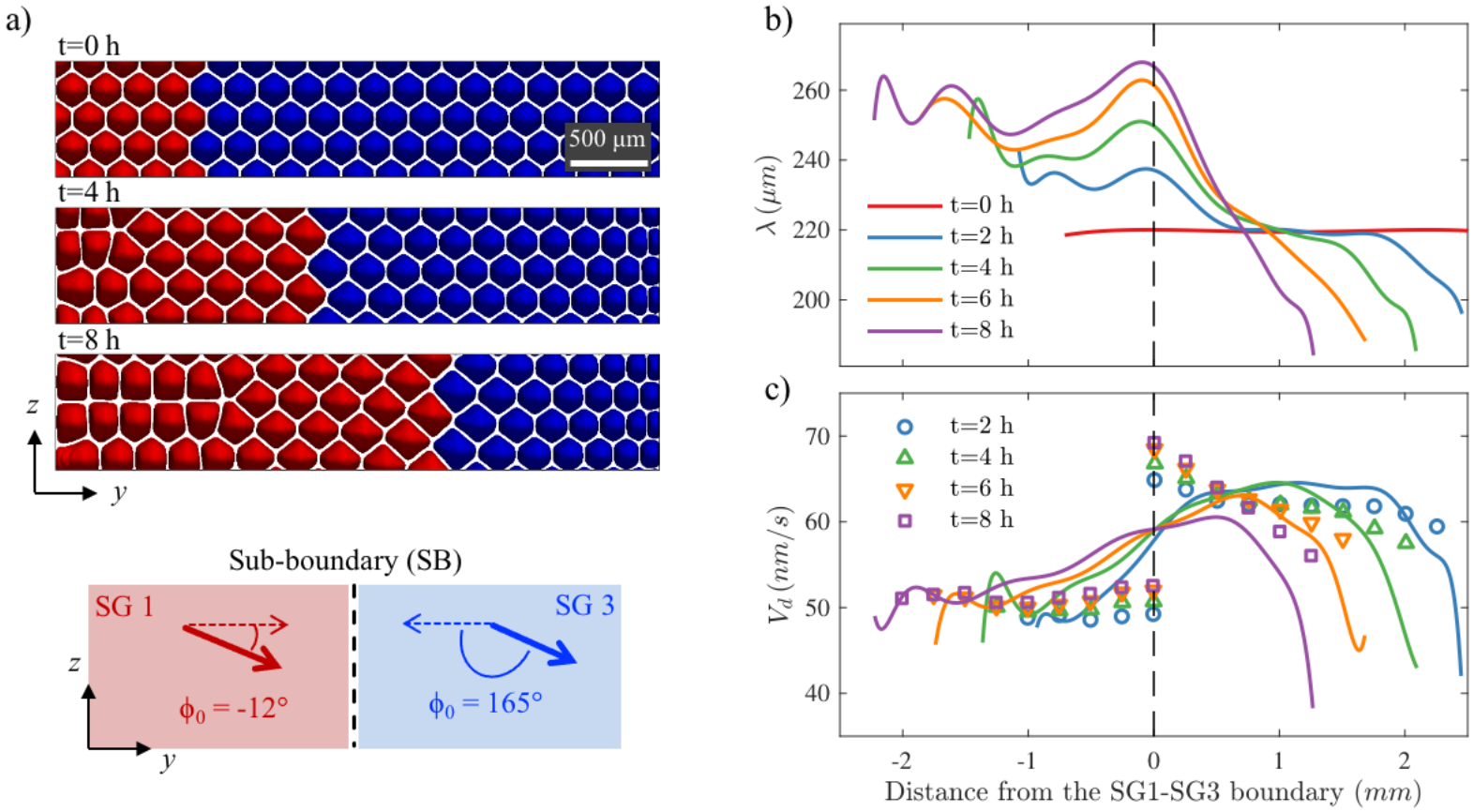

Figure(s)

FIGURE 14

Figure 14: Phase-field simulations with different initial D_{SB}, i.e., the distance from the source (the left boarder) to the SB. The values of initial D_{SB} are a) 923 µm, b) 1806 µm, and c) 2689 µm. Images in the top row show the initial and final microstructures. Videos are provided in supplementary material (videos 14a,1st and 2nd parts, of [61]).The distributions of spacing and V_d are shown in the second and third row.

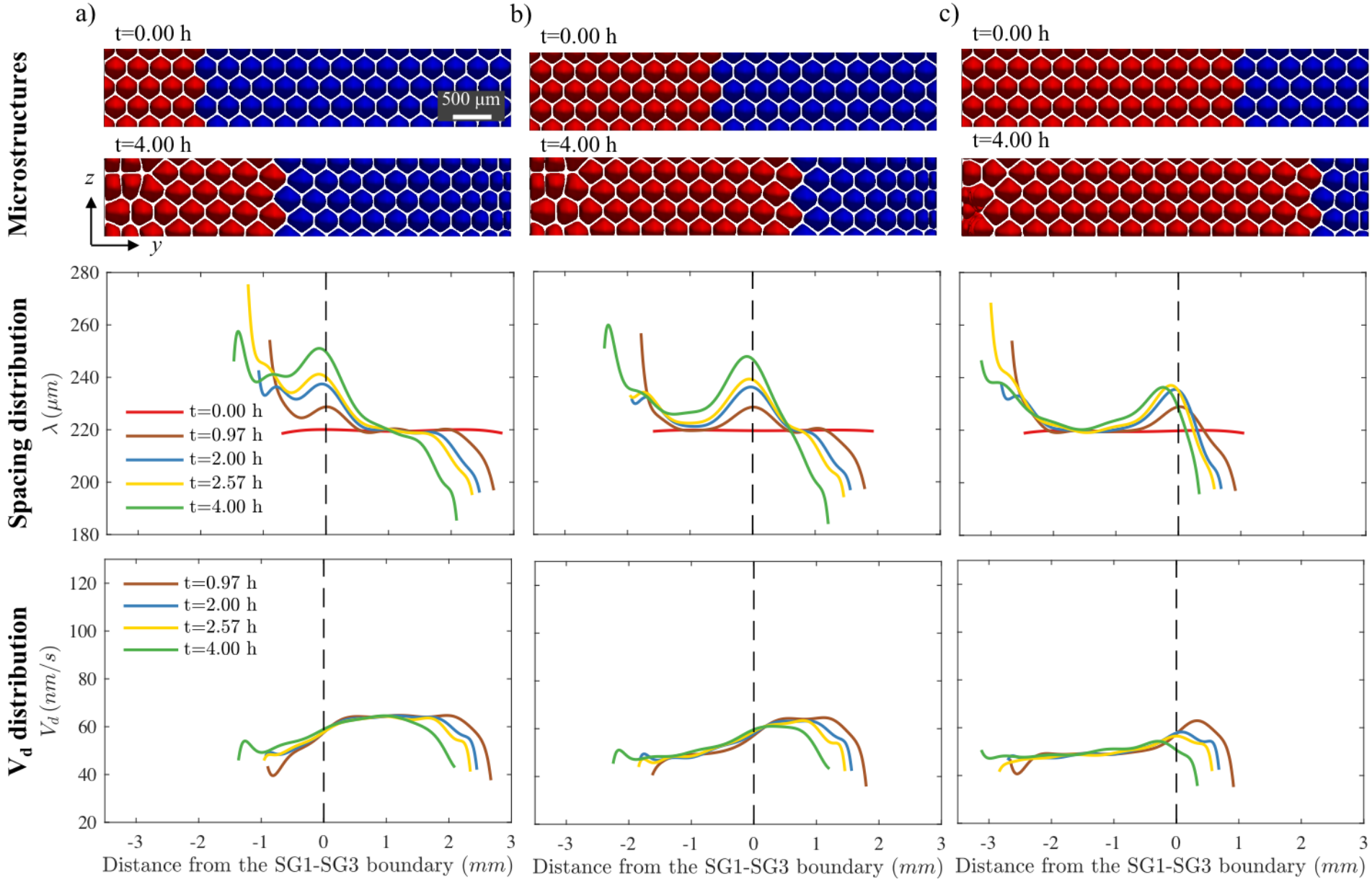

Figure(s)

FIGURE 15

Figure 15: Phase-field simulations for the convergent SB between SG 1 (left red grain) and SG 2 (right green grain) with different average spacing. The average spacing of the initial regular hexagonal array is a) 220 µm and b) 150 µm. Videos are provided in supplementary material (videos 15a and 15b of [61]). *The simulation domain size is a)* $L_x \times L_y \times L_z = 1495 \times 3960 \times 760\ \mu m^3$ *and b)* $L_x \times L_y \times L_z = 1495 \times 3900 \times 520\ \mu m^3$.

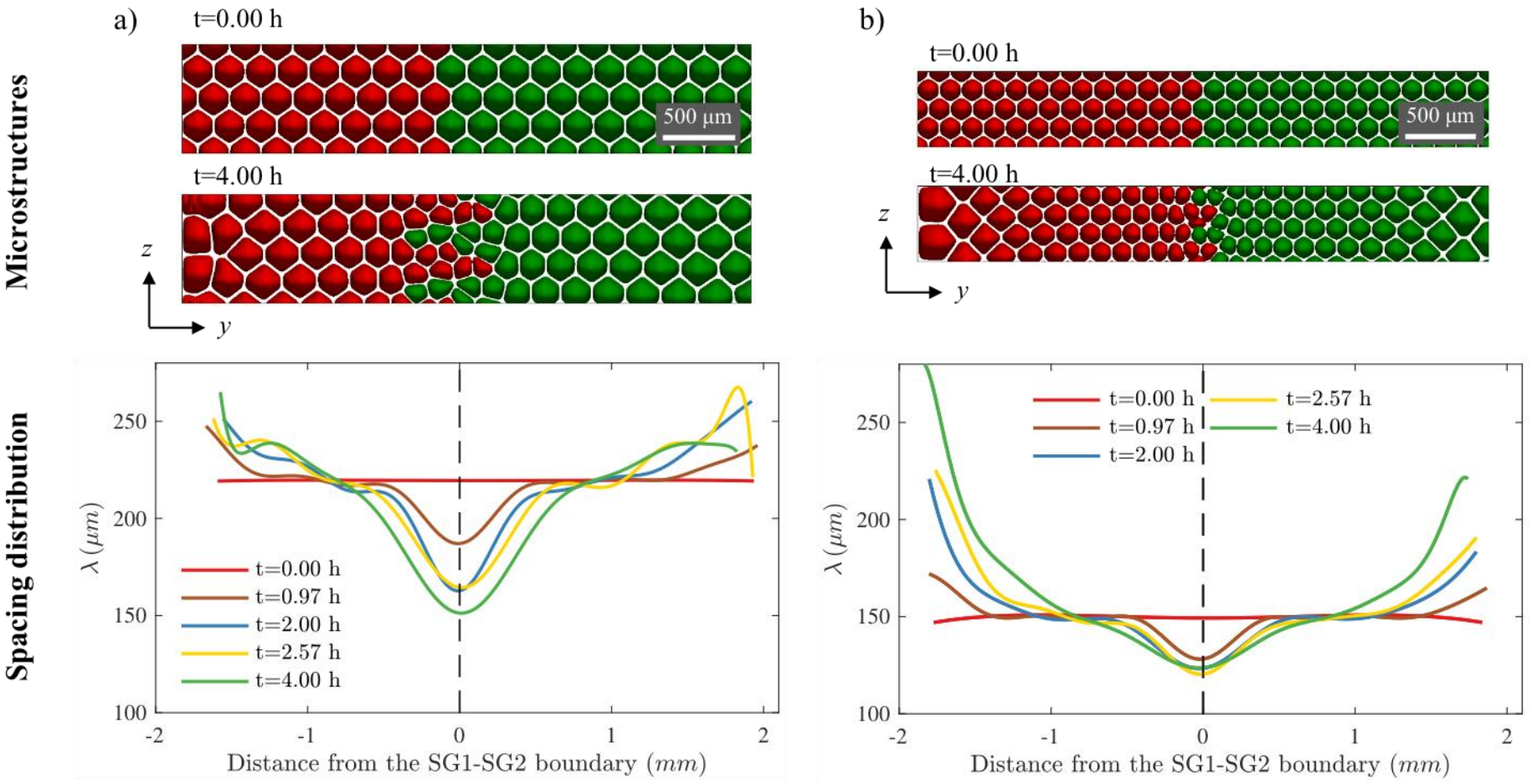

Figure(s)

FIGURE 9

Figure 9: Evolution of: (a) primary spacing map and (b) macroscopic interface shape, from *t* = 1 to 7 h. (SCN–0.24 wt % camphor, V_p = µm/s, G = 19 K/cm)

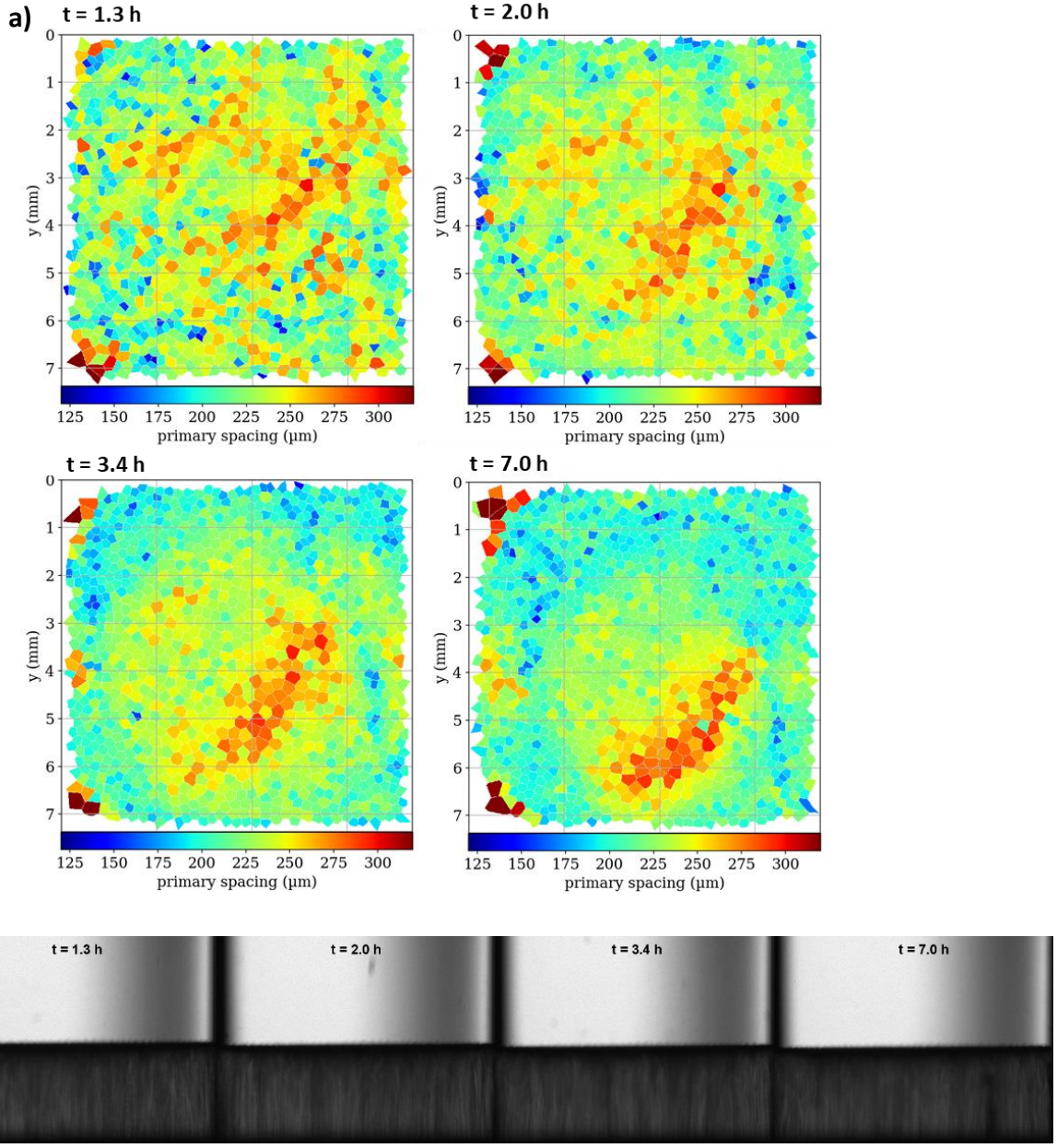

Click here to access/download
Supplementary Material
Mota et al_video1.avi

Click here to access/download
Supplementary Material
Mota et al_video14a.avi

Click here to access/download
Supplementary Material
Mota et al_video14b.avi

Click here to access/download
Supplementary Material
Mota et al_video15a.avi

Click here to access/download
Supplementary Material
Mota et al_video15b.avi

*Graphical Abstract

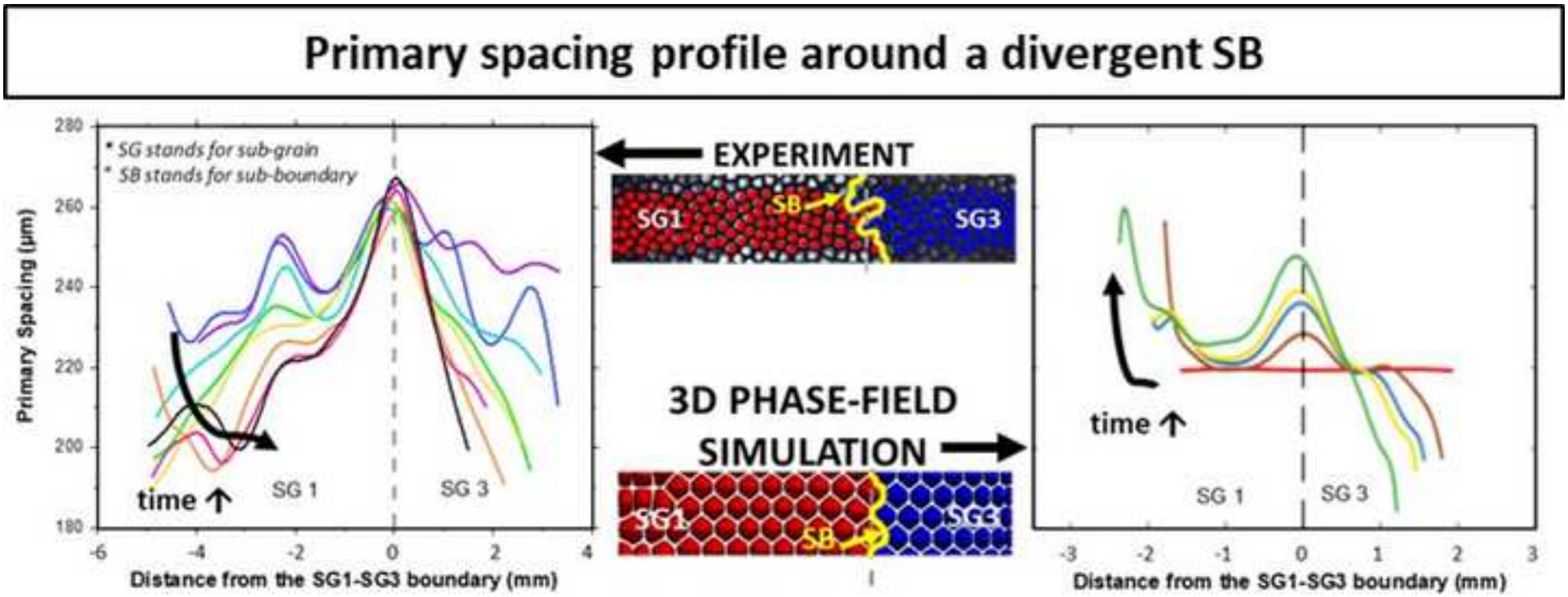

*Declaration of Interest Statement

Declaration of interests

☒ The authors declare that they have no known competing financial interests or personal relationships that could have appeared to influence the work reported in this paper.

☐The authors declare the following financial interests/personal relationships which may be considered as potential competing interests: